RICE UNIVERSITY

Manipulation of Energy Propagation, Redirection, and Dissipation by Tunable Plasmonic Nanostructures

by

Yang Li

A Thesis Submitted
in Partial Fulfillment of the
Requirements for the Degree

DOCTOR OF PHILOSOPHY

Approved, Thesis Committee:

Peter Nordlander, Chair
Professor of Physics and Astronomy;
Professor of Electrical and Computer Engineering

Naomi Halas
Stanley C. Moore Professor of Electrical and Computer Engineering; Professor of Chemistry; Professor of Physics and Astronomy

Stephan Link
Assistant Professor of Chemistry;
Assistant Professor of Electrical and Computer Engineering

Houston, Texas

October, 2012

Abstract

Manipulation of Energy Propagation, Redirection, and Dissipation by Tunable Plasmonic Nanostructures

by

Yang Li

Plasmons, the collective electronic oscillations of metallic nanoparticles and nanostructures, are at the forefront of the development of nanoscale optics. Metallic nanostructures with their geometry-dependent optical resonances are a topic of intense current interest due to their ability to manipulate light in ways not possible with conventional optical materials. As optical frequency nanoantennas, reduced-symmetry plasmonic nanoparticles have light-scattering properties that depend strongly on geometry, orientation, and variations in dielectric environment. Particularly fascinating aspect of these systems is the recently realized possibility of creating optical frequency "magnetic plasmon" responses of comparable magnitude to the "electric plasmon" response. It is of our central interest to understand better the plasmonic system so as to manipulate the energy transport mechanism.

With the much more advanced numerical calculations, and based on the Finite Element Method (FEM) and Finite-Difference Time-Domain (FDTD) method, we are now able to study various kinds of nanostructures for different interesting optical

properties.

With the help of FDTD, we show the geometry dependent dissipation rate in different nanosystems. We brought up a new damped harmonic oscillator model to account for the observed difference. We show that our new model better completes the full map of the energy dissipation mechanism, and the predicted outcome agreed very well with the FDTD calculations.

Elliptical nanorings were investigated by applying both FEM and FDTD methods. The mulitiple plasmonic resonaces exhibited by elliptical nanorings and the well tunability of the nanosystem make elliptical nanorings very interesting. Different features can be realized by controlling the aspect ratios of the elliptical nanorings.

We show another interesting nanostructures, light bending nanocup as well. Due to its unique light scattering properties, nanocup is a very promising candidate in solar cell applications. We studied more about its light redirection properties with the presence of a dielectric substrate and its sensitivity to the subtle geometry differences.

Plasmonic heptamer has been shown to possess an intriguing Fano resonance due to the interference of its hybridized subradiant and super-radiant modes. Neighboring fused heptamers can support magnetic plasmons due to the generation of antiphase ring currents in the metallic nanoclusters. We use such artificial plasmonic molecules as basic elements to construct low-loss plasmonic waveguides and devices. The manipulation of magnetic plasmons in heptamer interconnects can further be expanded to more complex systems, for example, by integrating more optical paths to achieve

multiple input and output plasmonic networks. With their compact dimensions, outstanding low-loss propagation characteristics, and range of functionalities, magnetic plasmon-based devices based on these structures should be key to the further development of high- performance energy transport components in informa- tion processing and data storage applications.

Acknowledgments

I would like to express my sincere gratitude to those people who have been helping and inspiring me during my study. My deepest gratitude goes to my advisor, Prof. Peter Nordlander. I have been amazingly fortunate to have an advisor who gave me the freedom to explore on my own, and at the same time the guidance to recover when my steps faltered. Peter taught me how to question thoughts and express my own ideas. His patience and support helped me overcome every single crisis situations and finish this dissertation. I am grateful to him for holding me to a high research standard and enforcing strict validations for each research result, thus teaching me how to do research. I would like to thank my thesis committee: Prof. Naomi Halas and Prof. Stephan Link for their valuable time in attending my thesis defense. Also, please let me show my thanks to my previous and current groupmates: Dr. Chizuko Dutta, Dr. Tamer Ali, Dr. Jorge Zuloaga, Dr. Heidar Sobhani, Dr. Ke Zhao, Dr. Nicolas Large, Dr. Kui Bao, Mr. Yurong Zhen, Mr. Yuming Wang, Mr. Vikram Kulkarni. Their helpful discussions are very important for the success of projects. My thanks also go to The Laboratory of Nanophotonics (LANP). This platform gives me great opportunities to broaden my knowledge and deepen my understanding in physics. Furthermore, please allow me to express my gratitude to other collaborators, Prof. Naomi Halas, Mr. Nicholas King, Mr. Ciceron Ayala-Orozco, Mr. Travis Brannan, Dr Na Liu, Dr Yangjun Cai, Prof. Paul Cremer for the pleasant disccusions and collaborations. Furthermore, my greatest gratitude goes to my lovely family for their

love and support throughout my life. Thanks to my parents, my lovely wife Ms. Jie Shu and our cute puppies Lebron and Olivia for always being there for me. In the last, I would like to thank all the funding agencies. This work is supported by the by the Robert A. Welch Foundation (C-1222) and the National Science Foundation (CNS-0421109).

Contents

Illustrations

Chapter 1

Introduction

With Finite Element Method (FEM) and Finite-Difference Time-Domain (FDTD) method, we theoretically investigated the optical properties of various metallic nanostructures, which can be easily tuned to realize the manipulation of energy propagation, redirection, and dissipation.

Using FDTD simulation, we find that for the given total number of electrons and resonant frequency, the spherical nanoshell possesses a broader linewidth than the ellipsoidal nanorod for LSPR excited along the long axis. By incorporating the retardation effect into the harmonic oscillator model for LSPR, we show that the geometries of nanoparticles strongly affect their linewidth through the geometric dependence of the dynamic depolarization, which renormalizes the electron mass and subsequently total energy of the oscillating electron gas. The scattering spectrum derived from our model agrees very well with the FDTD simulation, which consolidates our conclusion that elongated nanoparticles tend to possess narrower linewidths. Our findings can be important for the designing of plasmonic nanostructures.

Herein, a new and facile patterning method is demonstrated for the scalable fabrication of gold elliptical rings (ERs) in a controlled manner over large areas. Since the aspect ratio (AR) of the elliptical PS rings could be controlled by varying the applied strain during the capillary filling process, gold ERs with different ARs could

be fabricated in a scalable manner. The optical properties of the gold ERs were characterized by UV−vis/NIR and IR extinction measurements. The ERs exhibited only odd modes of polarization-dependent plasmonic resonances at normal incidence. The experiments and corresponding theoretical studies illustrated that all resonant modes could be tuned across a broad spectral range from the visible to the mid infrared (550−4700 nm) by simply varying the AR of the ERs. Moreover, the experimental data were confirmed by COMSOL simulations. We demonstrated both experimental and theoretical analysis of the optical properties of gold elliptical nanorings of different aspect ratios generated using stretched colloidal lithography. The plasmonic resonances are dependent on the incidence angle of light. At normal incidence, only odd-mode resonances are visible. At oblique incidence, dark-mode resonances become visible. Moreover, dark mode resonances are also dependent on the aspect ratio (AR) of the ERs. Both experimental and simulation data indicate that this phenomenon is due to a size–dependent retardation effect. All the resonance peaks over a wide range (500-5000nm) can be fitted into a simple standing wave model for quantitative prediction.

As optical frequency nanoantennas, reduced-symmetry plasmonic nanoparticles have light-scattering properties that depend strongly on geometry, orientation, and variations in dielectric environment. Here we investigate how these factors influence the spectral and angular dependence of light scattered by Au nanocups. A simple dielectric substrate causes the axial, electric dipole mode of the nanocup to devi-

ate substantially from its characteristic $cos^2\theta$ free space scattering profile, while the transverse, magnetic dipole mode remains remarkably insensitive to the presence of the substrate. Nanoscale irregularities of the nanocup rim and the local substrate permittivit y have a surprisingly large effect on the spectral- and angle-dependent light-scattering properties of these structures.

Neighboring fused heptamers can support magnetic plasmons due to the generation of antiphase ring currents in the metallic nanoclusters. We use such artificial plasmonic molecules as basic elements to construct low-loss plasmonic waveguides and devices. These magnetic plasmon-based complexes exhibit waveguiding functionalities including plasmon steering over large-angle bends, splitting at intersections, and Mach-Zehnder interference between consecutive Y-splitters. Our findings provide a strategy for circumventing significant challenges in the miniaturization and high-density integration of optical circuits in integrated optics, allowing for the development of ultracompact plasmonic networks for practical applications.

The thesis will be organized as follows: In Chapter 2, we will introduce a brand-new damped harmonic oscillator (HO) model for plasmonic systems by including the dynamic depolarization, and by applying this model, we will be able to successfully explain the geometry dependent damping mechanism, This improved HO model will be of great help for us to investigate the energy dissipation mechanism in plasmonic systems. The theory is consolidated by FDTD calculations. In Chapter 3, we investigate the plasmonic properties of elliptical nanorings (ER) with FEM and FDTD

calculations, which possess multiple plasmon resonances from visible to infrared regions. And all these resonances are strongly polarization dependent and could be tuned by varying the aspect ratios of the ERs. A standing wave model can simply be applied to analyze the resonances, which provides a simple designing guideline for potential applications in sensors and diagnosis. In Chapter 4, we use the FEM method to numerically calculate the optical properties of the light-bending plasmonic nanocups, We also observe effects of geometry and dielectric environment on the light scattering of plasmonic particles. The different scattering and wavelength response from both nanocup modes make nanocup an interesting particle for the nanoscale manipulation of light in three dimensions, such as enhancing the efficiency of solar cells. In Chapter 5, I will present magnetic plasmon formation and propagation in artificial plasmonic molecules, where antiphase magnetic plasmons are excited in adjacent heptamer units, supporting the propagation of low-loss magnetic plasmons in this new waveguide geometry. And by utilizing these heptamers as basic element, we construct low-loss magnetic plasmon based complexes, which exhibit waveguiding functionalities, such as plasmon steering, splitting, and Mach-Zahnder interference. The magnetic plasmon based devices will contribute a key role in the further development of high-performance energy transportation components for data storage and information processing applications. Finally, the conclusions of the thesis are in Chapter 6.

Chapter 2

Geometric Dependence of the Linewidth of Localized Surface Plasmon Resonance

2.1 Introduction

Metal nanoparticles possess the unique advantage of casting the various properties of light through localized surface plasmon resonance (LSPR), which makes them highly appealing candidates for nanoscale optoelectronic devices[15, 39, 57, 103]. The nanofabrication techniques rapidly developed throughout the last few decades have enabled the exquisite designing of nanoparticles and unprecendented tunability of their LSPR properties, such as their resonant frequency and linewidth, etc[3, 34, 48, 99, 104]. The LSPR properties are determined by several factors, including the material, geometry, and background dielectrics of the nanoparticles, as well as their coupling in both the classical and quantum regime[36, 118]. The influences of geometry on the LSPR properties have been extensively investigated and shown to be significant, indicating an important dimension for tuning LSPR.

The LSPR excited by external field quickly dephases, through both radiative and nonradiative channels, such as Landau damping and defect scattering. The dephasing time is manifested as the linewidth in the LSPR spectrum and plays a critical role in determining its Q-factor. While the previous works have investigated the geometric influence on the linewidth, they only compared nanoparticles with different total

number of electrons N_e and LSPR frequency ω_r[91, 117]. It is, however, important to fix these variables if we want to focus on the effects of different particle shapes, because at least the radiative damping increases with N_e and ω_r for the same shape of nanoparticles[31]. An equal-foot comparison of the LSPR linewidths of nanoparticles possessing the same N_e and ω_r , but only different shapes motivates our current work.

We perform finite-difference time-domain (FDTD) simulations and find that for the given volume and resonant frequency, the gold spherical nanoshell possesses a broader linewidth than the ellipsoidal nanorod for LSPR excited along the long axis of the rod. We explain this geometric dependence by incorporating the retardation effect into the harmonic oscillator model for LSPR. In our simple model, the geometries of nanoparticles are shown to strongly affect the linewidth through the geometric dependence of the dynamic depolarization, which renormalizes the electron mass and subsequently total energy of the oscillating electron gas. Moreover, the scattering spectrum derived from our model agrees very well with the FDTD simulation, which consolidates our conclusion that elongated nanoparticles tend to possess narrower linewidths. Our findings can be important for the designing of plasmonic nanostructures.

2.2 The harmonic oscillator model

We only consider the dipolar LSPR, where all electrons undergo harmonic oscillation when driven by the external electric field $\overrightarrow{E}_{ext}(t) = \overrightarrow{E}_0 e^{-i\omega t}$. For simplicity and

not losing generality, we only consider here axially symmetric nanoparticles with the external electric field polarized along its long axis, which is defined in the z direction. So $\overrightarrow{E}_0 = E_0\hat{e}_z$, where $\hat{e}_z$ is the unit vector along the z direction. The equation of motion for each electron is:

$$m\ddot{z} = -\tilde{K}z - m\gamma\dot{z} + m\gamma_{rad}\dddot{z} - e[\overrightarrow{E}_{ext}(t) + \overrightarrow{E}_p(t)], \tag{2.1}$$

where m and e are the electron mass and charge respectively, z is the deviation of electrons from their equilibrium position, $\tilde{K}$ is the phenomenological restoring coefficient for electrons due to positive ionic background, γ and γ_{rad} measure the intrinsic and radiative damping force, and $\overrightarrow{E}_p(t) = \overrightarrow{E}_p e^{-i\omega t}$ is the retarded electric field stimulated by local dynamic dipole moments. For the dipolar LSPR, we use the stimulated electric field at the center of the nanoparticle to represent the field applied on each local dipole moment, which turns out to be a sufficiently good approximation as verified by our FDTD simulation. The consequence of this approximation is that the motions of all electrons and their associated dynamic dipole moments in the nanoparticle are identical, which fits into the physical picture of rigidly oscillating electron gas. γ can either be measured experimentally or derived from quantum mechanical calculations accounting for different intrinsic damping mechanisms. The radiation damping coefficient is:

$$\gamma_{rad} = \frac{1}{6\pi\varepsilon_0}\frac{e^2}{mc^3}, \tag{2.2}$$

where ε_0 and c are the dielectric constant and speed of light in vacuum[45]. $\overrightarrow{E}_p(t) = E_p\hat{e}_z$, with the explicit expression of E_p derived from Hertzian dipole field[71]:

$$E_p = \int \frac{e^{ik\cdot r}}{4\pi\varepsilon_0}[\frac{k^2}{r}sin^2\theta + (\frac{1}{r^3} - i\frac{k}{r^2})(3cos^2\theta - 1)]PdV, \tag{2.3}$$

where $k = \frac{\omega}{c}$, r and θ are the radial distance and azimuthal angle in the spherical coordinate system, P is the dipole moment per unit volume, and dV is the differential element of volume. Retaining the orders of k up to the third, E_p can be explicitly expressed as:

$$E_p = (\mathbf{L} + k^2\mathbf{D} + ik^3\frac{V}{6\pi})\frac{P}{\varepsilon_0}, \tag{2.4}$$

where $\mathbf{L}$ and $\mathbf{D}$ are the static and dynamic geometrical factors respectively, and V is the volume of the nanoparticle. In particular,

$$\mathbf{D} = \frac{1}{8\pi}\int \frac{1}{r}(cos^2\theta + 1)dV, \tag{2.5}$$

Note that $\overrightarrow{E}_p(t)$ includes the essential many-body interaction and gives rise to the dynamic depolarization, which is missing in previous harmonic oscillator models for LSPR[75].

Since k is equivalent to $\frac{i}{c}\frac{d}{dt}$ for the harmonic oscillating system, we can recast Eq. (2.1) into the form of independent harmonic oscillators, by renormalizing the electron mass with dynamic depolarization and correcting the restoring and radiative

damping forces. By connecting x and P through the relation $P = -Nex$, where N is the number of electrons per unit volume, the recast equation is:

$$m^*\ddot{x} = -Kx - m\gamma\dot{x} + m\gamma^*_{rad}\dddot{x} - e\overrightarrow{E}_{ext}(t), \tag{2.6}$$

where the renormalized electron mass is:

$$m^* = m(1 + \frac{\omega_p^2}{c^2}\mathbf{D}), \tag{2.7}$$

and the corrected restoring and radiative damping coefficients are:

$$K = \tilde{K}(1 + \frac{\omega_p^2}{\omega_0^2}\mathbf{L}), \tag{2.8}$$

$$\gamma^*_{rad} = \gamma_{rad}NV, \tag{2.9}$$

with $\omega_p = \sqrt{\frac{Ne^2}{\varepsilon_0 c^2}}$ and $\omega_0 = \sqrt{\frac{\tilde{K}}{m}}$.

Based on Eq. (2.6), we can derive the linewidth in a simple and intuitive way. As a consequence of the mass renormalization, the resonant frequency of the oscillating electron gas is red-shifted to

$$\omega_r = \sqrt{\frac{K}{m^*}} = \sqrt{\frac{\omega_0^2 + \omega_p^2\mathbf{L}}{1 + \omega_p^2\mathbf{D}/c^2}}, \tag{2.10}$$

The time-averaged total energy of the oscillating electron gas at resonance is

$$< E >= 2\cdot < \frac{1}{2}m^*\omega_r^2 x^2 > \cdot NV = \frac{m^*\omega_r^2}{2Ne^2}|P|^2 V, \tag{2.11}$$

The time-averaged intrinsic and radiative dissipation powers are

$$- < \frac{dE}{dt} >_{intr} = < -m\gamma\dot{x}\cdot\dot{x} >= \frac{m\gamma\omega_r^2}{2Ne^2}|P|^2V^2, \tag{2.12}$$

$$- < \frac{dE}{dt} >_{rad} = < -m\gamma_{rad}^*\ddot{x}\cdot\dot{x} >= \frac{m\gamma_{rad}\omega_r^4}{2e^2}|P|^2V^2, \tag{2.13}$$

Note that Eq. (2.12) exactly agrees with the straightforward calculation of the energy flow outwards, when the interference of radiation from different parts of the nanoparticle is ignored. The linewidth of LSPR is thus

$$\Gamma = \Gamma_{intr} + \Gamma_{rad} = \hbar(\gamma + NV\omega_r^2\gamma_{rad})/(1 + \omega_p^2\mathbf{D}/c^2), \tag{2.14}$$

where Γ and $\Gamma_{intr(rad)} = -\hbar < \frac{dE}{dt} >_{intr(rad)} \cdot\frac{1}{<E>}$ denote the total linewidth and the contribution from intrinsic (radiative) damping respectively. Eq. (2.14) shows that the geometry affects the linewidth through its influence on the dynamic depolarization factor $\mathbf{D}$. It should be noted that Eq. (2.14) is accurate enough only when the damping is much smaller than the resonant frequency, i.e. $\Gamma \ll \omega_r$. For large damping, not only Γ deviates from $\hbar(\gamma + NV\omega_r^2\gamma_{rad})/(1 + \omega_p^2\mathbf{D}/c^2)$, but also ω_r is shifted from $\sqrt{(\omega_0^2 + \omega_p^2\mathbf{L})/(1 + \omega_p^2\mathbf{D}/c^2)}$. Both the exact resonant frequency and

linewidth should be obtained from the scattering spectrum, which can be calculated by the dynamic polarizability $\alpha(\omega)$ of the nanoparticle:

$$\alpha(\omega) = \frac{V\varepsilon_0\omega_p^2/(1+\omega_p^2\mathbf{D}/c^2)}{(\omega_0^2+\omega_p^2\mathbf{L})/(1+\omega_p^2\mathbf{D}/c^2)-\omega^2-i\omega(\gamma+NV\omega^2\gamma_{rad})/(1+\omega_p^2\mathbf{D}/c^2)} \quad (2.15)$$

The corresponding scattering cross section is[11]:

$$\sigma_{scat}(\omega) = \frac{\omega^4}{6\pi\varepsilon_0^2c^4}|\alpha(\omega)|^2 \quad (2.16)$$

Note that Eqs. (2.10) and (2.14) agree exactly with Eq. (2.15) for sufficiently small damping.

2.3 The comparison between nanorod and nanoshell

We compare different pairs of gold ellipsoidal nanorod and spherical nanoshell, each pair possessing the same ω_r while N_e being kept identical for all the structures. This is achieved by adjusting the aspect ratio of the nanorod, and inner and outer radius of the nanoshell. We take $\omega_p = 8.94eV$ and $\gamma = 0.069eV$ for both the analytical model and Drude dielectric function $\varepsilon(\omega) = \varepsilon_\infty - \omega_p^2/\omega(\omega+i\gamma)$ for our FDTD simulation, which is carried out by the commercial software FDTD Solutions. The background dielectric constant ε_∞ is taken as 9.5. In addition, because the dipolar and higher order multipole LSPR are very close to each other in nanoshells, calculations based

on Mie theory are carried out to extract the linewidth of their dipolar LSPR only[11]. Throughout the whole study, the external electric field is polarized along the long axis of the nanorod. One particular comparison of the scattering cross section of one pair is illustrated by Fig. 2.1. Because of the generally broad linewidth in the nanostructures currently studied, the spectrum deviates significantly from the Lorentzian lineshape and we extract the linewidth by measuring the frequency difference between the two half-maximum points on the spectrum, both here and for the rest of the chapter.

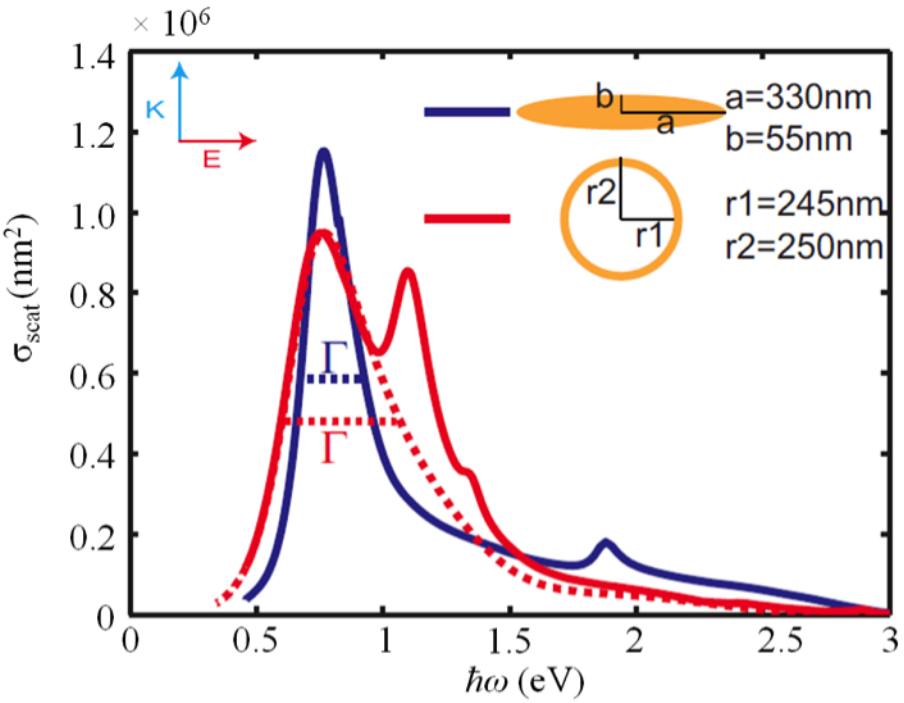

Figure 2.1 : Spectrum of scattering cross section for a nanorod (blue) and a nanoshell (red). Solid lines are results of FDTD simulation and the dashed line is calculated by Mie theory including only the dipolar mode. The aspect ratio of the nanorod is a/b = 330nm/55nm = 6, while r_1 = 245nm and r_2 = 250nm for the nanoshell. For the nanorod, the incident light propagates along its short axis with the polarization along the long axis.

A systematic comparison of different pairs of nanorod and nanoshell is shown in

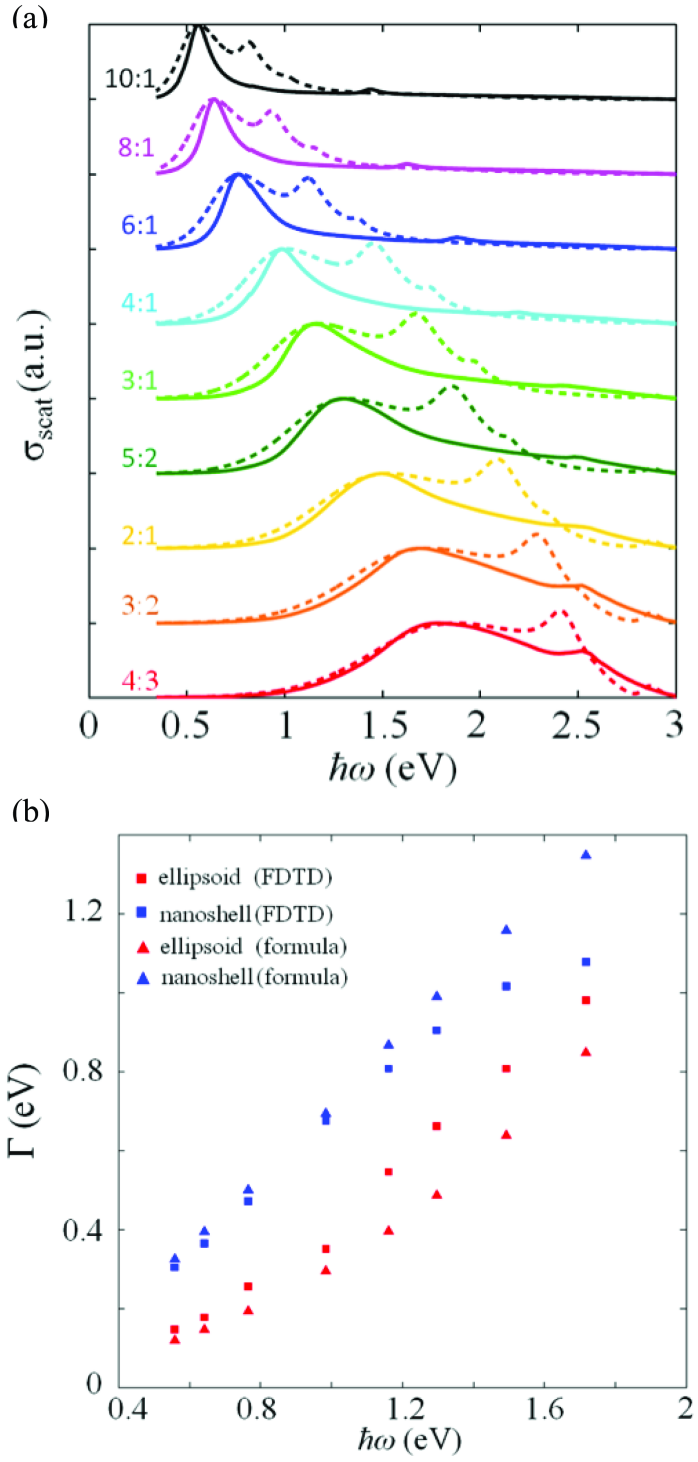

Figure 2.2 : (a) Normalized spectrum of scattering cross section for nanorods (solid lines) and nanoshells (dashed lines). The aspect ratios of nanorods increase gradually (4:3, 3:2, 2:1, 5:2, 3:1, 4:1, 6:1, 8:1, 10:1). The corresponding inner and outer radii of nanoshells are: (80, 115), (97, 124), (120, 140), (145, 159), (165, 176), (192,201), (245, 250), (286, 290), (318, 321) in nm. (b) Linewidths extracted from FDTD simulations (squares) and calculated by Eq. (2.14) (triangles).

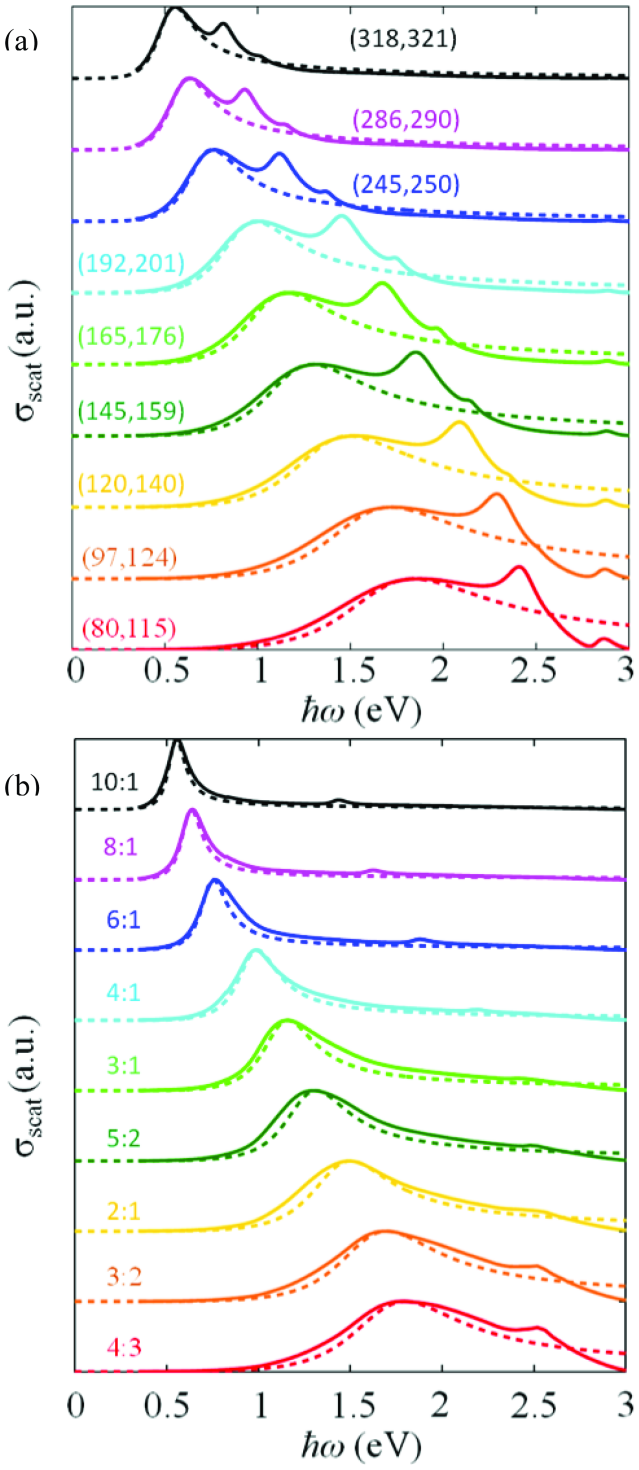

Figure 2.3 : Spectrum of scattering cross section of (a) nanoshells and (b) nanorods, calculated by FDTD (solid lines) and Eq. (2.16) (dashed lines).

Fig. 2.2(a) and (b). For an easy visualization, each spectrum is normalized so that the dipolar resonance peak is unity, and the spectra of different pairs are shifted from each other. For the nanorod with the aspect ratio of 4:3, its dipolar and quadrupolar LSPRs are so close that the measured linewidth is no longer valid for dipolar LSPR, which is the reason why we do not include this pair for Fig. 2.2(b). The FDTD simulation shows that for each pair, the linewidth of the nanoshell is clearly broader than that of the nanorod, and this difference tend to diminish when the aspect ratio of the nanorod is close to one as the two structures are getting similar to each other. The linewidth acquired from Eq. (2.14) agrees well with the FDTD results, especially at low energy end and the discrepancy in the high energy regime is a result of very broad resonant peaks.

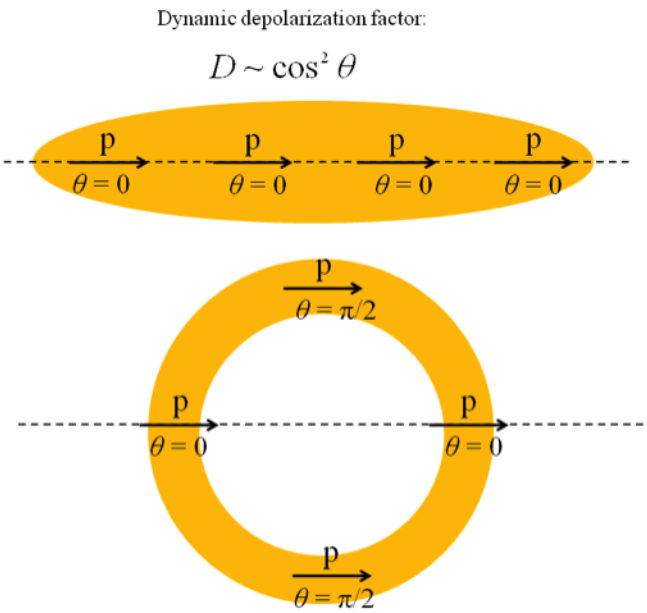

Figure 2.4 : Schematic of representing the nanorod and nanoshell with four dipole moments, to show the effect of different geometry on the dynamic depolarization.

Figures 2.3(a) and (b) compare the scattering spectrum acquired by FDTD simulation and Eq. (2.16) for nanoshells and nanorods respectively, and the very good agreement confirms the validity of Eq. (2.14). The effect of the shape of a nanoparticle on **D**, and subsequently the linewidth, can be conceptually understood by a simple analogy: if we represent the nanoshell and nanorod by four dipole moments as illustrated by Fig. 2.4, the θ for the nanoshell is 0 for two dipoles and $\pi/2$ for the other two, while for nanorod, all $\theta = 0$, which makes the nanoshell possess a narrower linewidth when Eq. (2.5) is considered. This simple picture also indicates that elongated nanoparticles tend to have a narrower linewidth than more isotropic ones.

2.4 Summaries and conclusions

In conclusion, using FDTD simulation, we find that for the given total number of electrons and resonant frequency, the spherical nanoshell possesses a broader linewidth than the ellipsoidal nanorod for LSPR excited along its long axis. We explain this phenomenon by incorporating the retardation effect into the harmonic oscillator model for LSPR. We show that the geometries of nanoparticles strongly affect their linewidth through the geometric dependence of the dynamic depolarization, which renormalizes the electron mass and subsequently total energy of the oscillating electron gas. The scattering spectrum derived from our model agrees very well with the FDTD simulation, which consolidates our conclusion that elongated nanoparticles tend to have

narrower linewidths. Our findings can be important for the designing of plasmonic nanostructures.

Chapter 3

Elliptical Nanorings with Highly Tunable and Multiple Plasmonic Resonances

3.1 Introduction

The interaction of metallic structures with electromagnetic radiation depends strongly on a particle's geometry, which is associated with localized surface plasmon resonances (LSPR). Specifically, the effects of size, periodicity, and morphology have stimulated substantial interest in experimental and theoretical research, which in turn has led to a wide range of applications, including chemical and biological sensors,[28, 56] photonics,[108] surface-enhanced spectroscopy,[1, 10, 16, 50, 94] and the development of metamaterials.[21, 87, 92] One of the challenges is to widely tune the LSPR for specific applications. For example, it has been found that peak intensities from surface enhanced Raman spectroscopy (SERS) and surface enhanced infrared absorption spectroscopy (SEIRAS) are dependent on the particular geometries of the nanostructures. Generally, optimal enhancement and signal generation can be achieved when the LSPR resonances of the nanostructures are tuned to match the excitation wavelength of adjacent molecules of interest.[1, 114] In addition, for planar nanostructures, only dipolar resonances could be excited at normal incidence. However, higher order resonances have more uniform E-field distributions due to a larger number of nodes, which can be particularly useful for SERS measurements and sensing applications.[88]

Therefore, it is highly desirable to generate nanostructures with multiple, highly tunable, and predictable LSPR resonances over a wide wavelength range.

In previous studies, considerable effort was put into understanding the behavior of circular nanorings. This is because of the ease of fabrication and tunable plasmonic properties, which are desirable for a variety of applications.[2, 9, 40, 46, 52, 55, 79, 100, 109, 110] For example, nanorings have a uniformly enhanced electric field inside a circular cavity, which has been shown to be suitable for biosensor development.[2, 52] On the other hand, rings with reduced symmetry (symmetry-breaking) have been fabricated by the introduction of gaps or asymmetric widths into the symmetric ring structure. Such reduced symmetry should exhibit unique optical and magnetic properties that are not available with symmetric structures. A common asymmetry geometry is the split-ring, first proposed by Pendry et al.,[80] which has prompted a wide range of applications.[16, 28, 27, 90] Recently, Nordlander et al. proposed ring structures with asymmetric gaps, which exhibit asymmetric Fano resonances and unusually large LSPR sensitivity.[40] Such elements could be potentially applied in new types of optical devices and sensors. An alternative strategy for introducing asymmetry into circular rings involves elongating them into elliptical rings. ERs have shown unique properties in magnetic materials compared with their symmetric ring counterparts.[19]

Herein, we developed a scalable method for ER production over large areas, which allowed for the generation of ERs with varying aspect ratios by using a single PDMS

stamp. The plasmonic resonances of these structures could be tuned in a predictable manner as the aspect ratio of the ERs was varied. Moreover, varying the ring widths along the perimeter of the ERs allowed multipolar resonances to be excited. These ranged in frequency from the visible to the mid- IR and were highly polarization dependent.

However, we only observed odd-mode resonances at normal incidence. Previous papers have shown that retardation effect could also cause the excitation of high-order resonances. Retardation effects take effect when the size of nanostructures is comparable to the wavelength of the incidence light. As such the electric field is not uniform across nanostructures and high order resonances could be excited. For planar nanostructures, previous papers have shown that oblique incidence could excite multiple resonances of, for example, nanorings. In this chapter, we also investigate the optical properties of ERs at the oblique incidence. We found that in addition to the bright resonances observed at normal incidence, dark-mode resonances could be excited at oblique incidence. Meanwhile, we found that the excitation of dark-mode resonance is also dependent on the incidence angle and aspect ratio of ERs. The calculated data exhibit excellent agreement with the experimental results. Similar to the bright resonances, dark-mode resonances are also able to be fitted to standing wave model for predicting resonances.

3.2 Results and Discussions

3.2.1 Simulation Setup

Theoretical data for ERs were calculated numerically using commercial finite element modeling (FEM) software (COMSOL Multiphysics 4.2 with the 3D RF module). In the calculation, a single nanostructure was defined in the simulation domain, an incident plane wave at the experimental incidence angle was defined, and the scattered field was solved by using the Stratton-Chu formula. The procedure was repeated over a set of wavelengths to compile a full scattering spectrum. Perfectly matched layer (PML) was used to eliminate numerical artifacts at the simulation boundary. The Au nanoring was modeled as an elliptical nanoshell with a concentric elliptical air core. The core axes were set to w_L and w_S, respectively, to match the average parameters in the experiment, while the outer axes of the nanoring were D_L and D_S. A Drude fitted dielectric function $\varepsilon = \varepsilon_\infty - \frac{\omega_B^2}{\omega^2 + i\gamma\omega}$ was employed to model the gold nanoparticles. Here, the background dielectric constant $\varepsilon_\infty = 9.5$, the bulk plasma frequency $\omega_B = 8.94eV$, and the intrinsic damping parameter $\gamma = 0.069eV$ were employed. The charge density plots for the elliptical nanorings were also obtained by COMSOL and the coloring was adjusted for contrast.

To investigate the effect of periodicity introduced by the fabrications on the optical properties of ERs, Lumerical FDTD calculations were also performed. Same PML and drude dielectric functions for gold were applied. Differently, here we applied periodic boundary conditions (PBC) in the structures. As later in this chapter (Fig

3.4) presents, a unit cell of the periodic structure was picked and PBC was applied right at the boundaries of this unit cell. In this case, we were able to investigate the optical properties of the ER arrays, which were actually more close the real geometry.

3.2.2 Optical Properties of the ERs

Figure 3.1a shows the extinction spectra (400−5000 nm) of Au ERs with AR values of 1.0, 1.17, 1.53, 1.84, 2.10, 2.72, and 3.70. The spectra in red are from light with the electric field polarized along the long axis, while the blue spectra are for light polarized along the short axis. As expected, the spectra of circular rings (AR = 1.0) are identical for the two polarizations (Figure 3.1a). The circular rings exhibited three distinct peaks at 2100, 1022, and 650 nm. The plasmon modes of metallic ring structures can be classified according to their azimuthal symmetry m (where m ranges from 1 to infinity) and the relative charge alignment on the inner and outer surfaces (symmetric or antisymmetric) of the ring wall. According to previous studies,[2, 100, 109] circular rings generally exhibited two resonance peaks: a symmetric bonding dipolar and an asymmetric antibonding plasmon mode. The bonding dipolar mode with its electric field extending over the whole structure is highly tunable and depends sensitively on the geometrical parameters of the structure.[33] In contrast, the antibonding mode with its electric field localized within the ring wall is only weakly tunable and depends primarily on the ring width w. The strong peak at 2100 nm has been assigned to the symmetric dipolar resonance (or the mode-1 resonance: $m = 1$), while the peak

at 650 nm was ascribed to the antibonding resonance along the width of the circular rings (λ_w).

In the present work, an unexpected weak peak was also found near 1022 nm and has not been previously assigned. This mode is barely visible for circular rings at normal incidence and is a dark higher order multipolar resonance.[40]Such dark-mode resonances should become significantly more intense when the symmetry of the nanostructures is broken.[40, 74, 79] For example, it has been recently reported that asymmetric theta-shaped ring-rod Au nanostructures[38] and nanorings with asymmetric widths[40] exhibited dark-mode resonances at normal incidence. In the present case, two possible symmetry-breaking factors may contribute to the appearance of the 1022 nm peak. First, the ring width of circular rings may not be perfectly uniform along the perimeter of the rings due to fabrication defects, which may result in the excitation of dark mode resonances.[40] Second, the surfaces of Au nanorings will not be perfectly smooth after chemical wet etching, which may also result in symmetry breaking and therefore enable excitation of darkmode resonances at normal incidence.[74]

While circular rings gave rise to polarization independent extinction spectra, the spectra from the ERs exhibited significant polarization dependence (Figure 3.1a). For ERs, there are polarizations along both the long and short axes, which are referred to as “L” and “S” polarization, respectively. Like circular rings, the 650 nm peaks in the spectra for all the ERs can be attributed to the antibonding resonances along the

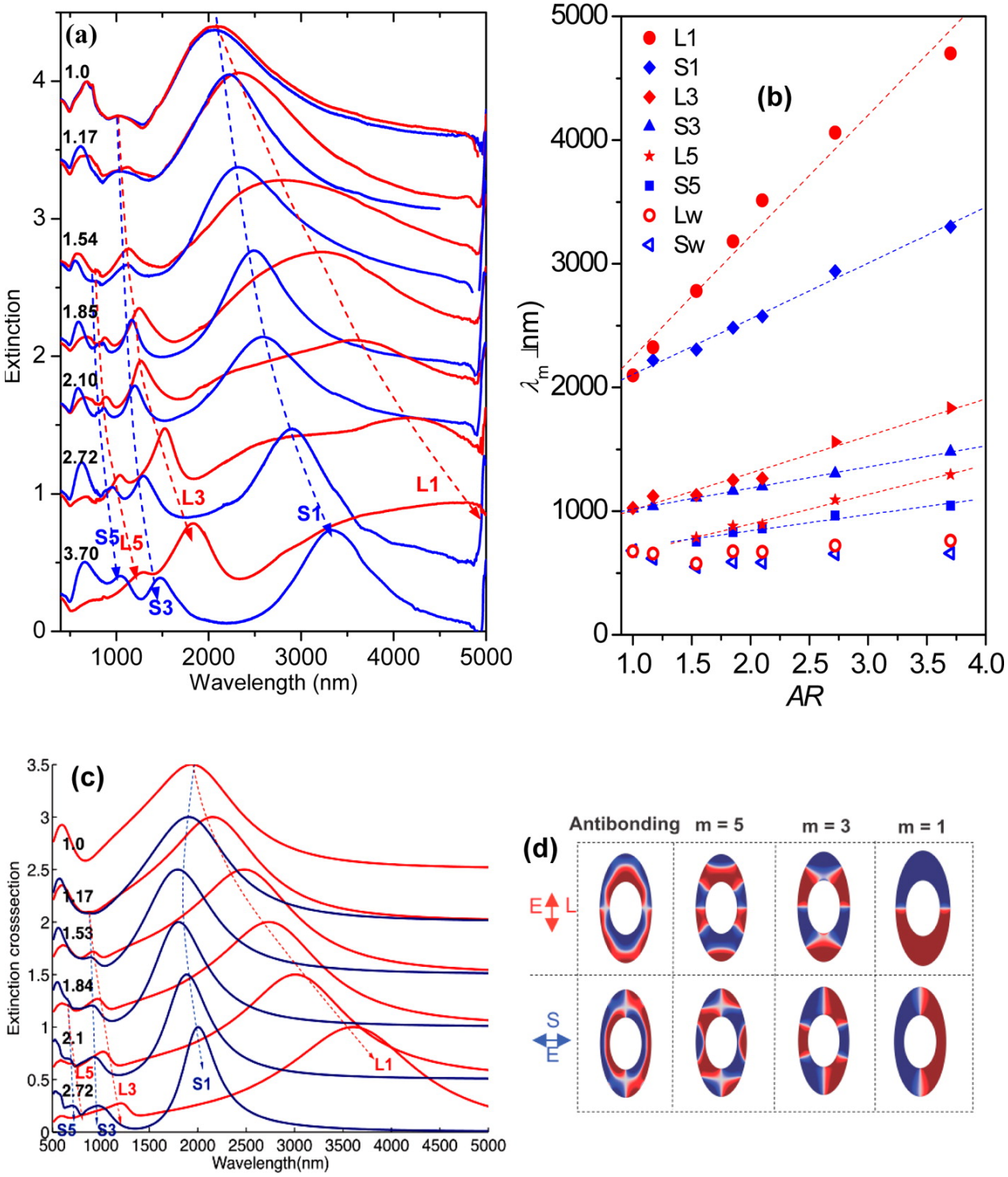

Figure 3.1 : (a) Extinction spectra of the ERs with the ARs of 1.0, 1.17, 1.53, 1.84, 2.10, 2.72, and 3.70, respectively, for L (red) and S (blue) polarizations. (b) The wavelength, λ_m, of the resonance peaks of different modes ($m = 1, 3, 5$, and antibonding modes L_w and S_w) and polarizations (S and L) versus AR. (c) Comsol simulation of the extinction spectra of ERs with AR from 1.0 to 2.72 for L (red) and S (blue) polarizations. (d) Charge distribution profiles of the corresponding resonances for AR = 2.10 in part c. The dashed lines in parts a and c are used to highlight the varying position of the resonance peaks of the same order of mode and polarization with increasing AR.

width of the structures.

The lowest energy features can be assigned to bonding dipolar resonances of the ERs and are labeled as S1 and L1 in Figure 3.1a. Both modes continuously red-shifted as the aspect ratio was increased. In addition to the dipolar bonding and antibonding resonances, ERs also exhibited higher order resonances for each polarization. For ERs with an AR of 1.17, only one higher order resonance appears for each polarization, and is labeled L3 and S3, respectively. Interestingly, as the AR was increased to 1.54 and beyond, one additional weak resonance was found for each polarization, and is labeled L5 and S5. Similar to the dipolar resonances, these high-order resonances also red-shifted when the polarization was switched from S to L ($\lambda_{S3} < \lambda_{L3}$ and $\lambda_{S5} < \lambda_{L5}$). Moreover, the observed intensities of the higher order resonances increased with increasing aspect ratio. As noted above, higher order resonances should be the result of symmetry breaking. This may be attributed to two factors: one is the anisotropic shape of the ERs, and the other is the difference between w_L and w_S. As the AR increased, the extent of symmetry-breaking increased, leading to increasing intensities of the higher order resonances. In addition, the resonances for the same order of mode and polarization (L1, S1, L3, S3, L5, and S5) red-shifted with increasing AR, as revealed by the dashed arrows in Figure 3.1a.

The extinction maxima as a function of AR for the spectra in Figure 3.1a are plotted in Figure 3.1b. As can be seen, the resonance wavelengths increased almost linearly with increasing AR. However, the antibonding resonances did not show a

significant red-shift by increasing the AR. It should be noted that all the above resonances are assigned odd azimuthal mode numbers m = 1, 3, and 5. Similar phenomena have been observed in nanowires, in which only odd-mode resonances were observed at normal incidence.[74, 85] This is in agreement with theory, as discussed below. Even mode resonances can also be excited but require off normal incidence excitation.

To analyze the experimental results in Figure 3.1a and b, we performed COMSOL simulations of the optical cross section of a single ER. Figure 3.1c shows the simulated spectra for an ER with ARs ranging from 1.0 to 2.72. The charge distribution profiles of the corresponding resonance peaks for AR = 2.10 are shown in Figure 3.1d. The antibonding resonances in the simulated spectra are in good agreement with the experimental data. Their charge distribution profiles (left two panels in Figure 3.1d) confirm the antisymmetric alignment expected for antibonding modes. For circular rings, only the dipolar resonance was observed. By contrast, dipolar resonances and higher order resonances were observed in the spectra of ERs for both polarizations. On the basis of the charge distribution profiles of the dipolar and high-order resonances, the order of the resonance modes (m) can be calculated to be half of the number of nodes (i.e., $m = n/2$) in the ERs. For example, because the higher order resonance in the L-polarization has six nodes along the perimeter of the ER, the resulting order of mode is 3, which is consistent with the assigned mode in Figure 3.1a.

The simulation data in Figure 3.1c show that all dipolar and multipolar reso-

nances, except S1 resonances, red-shift with the increase of AR. This is mostly consistent with the experimental results. However, the S1 resonances in the simulation first blueshifted slightly and then red-shifted as the AR increased further. This will be qualitatively explained below using a simple standing-wave model. Moreover, the resonances in the simulations, especially the S1 and high-order resonances, exhibited clear blue-shifts compared to the experimental results. There are several reasons for this deviation from the experimental data. First, the experimental data were measured from 2D arrays of ERs, while the simulations only calculated extinction spectra from a single ER. The coupling between ER elements in the experiments could induce the red-shift of the plasmonic resonances, which has been observed for circular nanorings.[46] Moreover, this coupling effect strongly depends on the pitch of the 2-D arrays or the gap between adjacent rings. For the ER arrays, the gap distance increased by $(1+\varepsilon)$ along the long axis but decreased by $(1-\varepsilon/2)$ along the short axis. This may explain why the S1 resonances in the simulation blueshifted as compared to the resonances in experiments, while the L1 resonances almost matched the experimental data. Second, the roughness of the Au surface in the experiments could produce a red-shift of resonances, which was not taken into account in the simulations. Indeed, this phenomenon has been observed in Au nanodots[8] and nanocrescents.[101] Third, the glass substrate in the experiment was not included in the simulation. Finally, the cross sections of the ERs were not perfectly rectangular as assumed in the simulations. Generally, due to isotropic wet etching of Au, they

were narrow on the top and wide at the bottom, resulting in trapezoidal or even triangular shapes. The asymmetric cross-sectional shapes could also cause red-shifting of the resonances.[109]

3.2.3 Standing-wave model

In order to quantitatively understand the shift of the resonance peaks, we employed a simple standing-wave model originally introduced to analyze the plasmonic resonances of a linear antenna of finite length l:[73, 51]

$$L = m\lambda_m/2n \tag{3.1}$$

In this expression, λ_m is the wavelength of the resonance of mode index m and n is the refractive index of the surrounding medium. This simple model has also been extended to other metallic ring structures which are then considered as linear antennas of lengths equal to the circumference of the ring.[21, 79, 107] In the most general case, the multiple plasmon resonances of a closed ring-like structure such as an ER can be obtained from a modified standing wave model:[21]

$$l_{eff} = \frac{m(\lambda_m + \lambda_0)}{2n_{eff}} \tag{3.2}$$

where l_{eff} is the effective length of the structure in the polarization direction and λ_0 depends only on the geometric structure.[21]

LSPR resonances of closed square rings of total perimeter lengths C have been

shown to be independent of polarization because the effective length, $l_{eff} = C/2$, is independent of polarization.[107] The polarization-independent spectra of the closed circular rings (AR = 1.0) in Figure 3.1a confirm this finding. By contrast, the spectra from ERs were polarization dependent. This is due to the fact that leff in eq 3.2 is different in the L and S directions. For an elliptical ring with long and short axes diameters of D_L and D_S, the half length of the perimeter is

$l = (\pi/4)\sqrt{2(D_L^2 + D_S^2) - (D_L - D_S)^2/2}$

For the L polarization, the electrical field (E) is parallel to the long axis of the ERs and the electrical currents oscillate between the two ends of the long axis (schematic diagram in Figure 3.2a). Therefore, the effective length l_L in the L direction can be calculated by substituting D_S by the inner diameter at the short axis ($D_S - 2w_S$):

$$l_L = (\pi/4)\sqrt{2(D_L^2 + (D_S - 2w_S)^2) - (D_L - (D_S - 2w_S))^2/2} \tag{3.3}$$

Similarly, the effective length l_S in the S direction can be calculated by substituting D_L by the inner diameter along the long axis ($D_L - 2w_L$):

$$l_S = (\pi/4)\sqrt{2((D_L - 2w_L)^2 + D_S^2) - ((D_L - 2w_L) - D_S)^2/2} \tag{3.4}$$

The values of l_L and l_S are plotted as a function of AR in Figure 3.2a. As expected, l_L is larger than l_S because $w_L > w_S$. Therefore, as expected from eq 3.2, the resonances red-shifted when the polarization was switched from S to L.

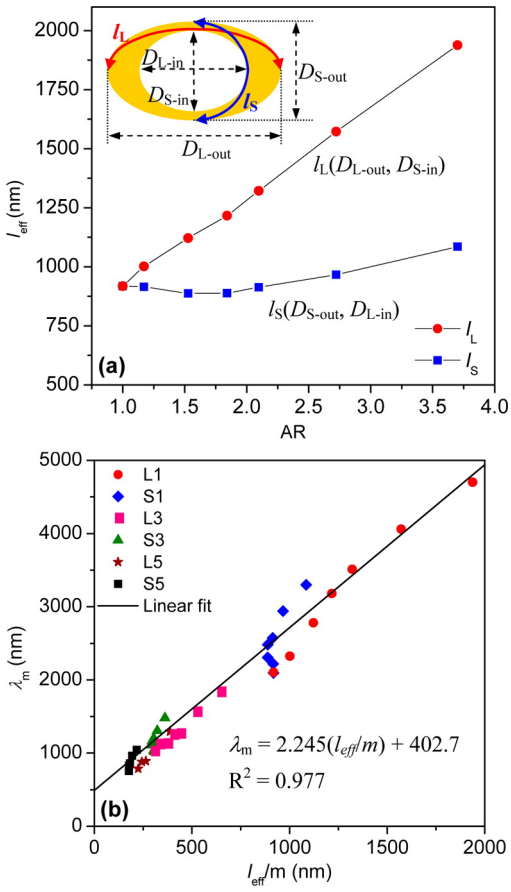

Figure 3.2 : (a) Plot of the effective path length l_{eff} (l_L and l_S) of the currents in ERs induced in two polarizations (L and S) as a function of AR. The schematic diagram shows that l_L can be calculated on the basis of D_{L-out} and D_{S-in} and l_S can be calculated on the basis of D_{S-out} and D_{L-in}. (b) Plot of wavelengths of multiple resonant peaks of different modes (m = 1, 3, and 5) and polarizations (L and S) as a function of l_{eff}/m. The solid line is a linear fit.

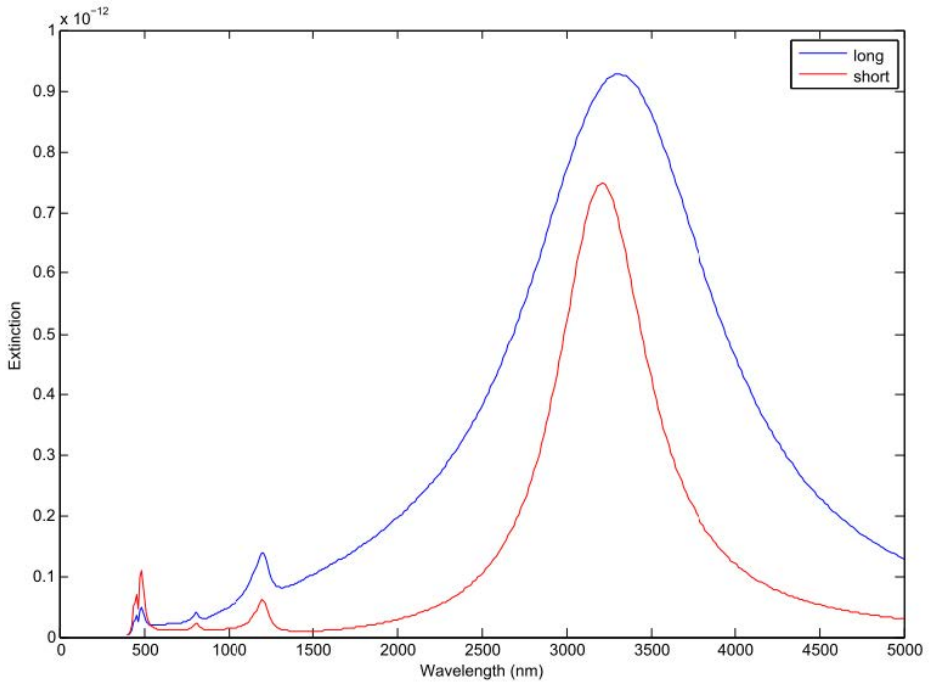

Figure 3.3 : Theoretical extinction spectra of an ER shown in the inset scheme. The ER has the same size as the ER (AR =1.84) except that the ring width is uniform (50 nm) instead of varying along the perimeter of the ER. The dipolar resonances for the L and S polarizations are 3290 nm (λ_L) and 3200 nm (λ_S), respectively, which indicates that the spectra of this ER are almost polarization independent as compared to the spectra in Figure 3.1. Also, the higher order multipolar resonances for the L and S polarizations are also quite close. This could be due to the fact that the two path lengths of the induced dipoles for the two polarizations are almost the same and equal to half of the perimeter of the ER. According to Eqs. (3.4) and (3.5), l_L and l_S can be calculated to be 1321 and 1296 nm, respectively, which are very similar. This explains the close resonance positions for the two polarizations. We believe that if the thickness further decreases, the dipolar resonances will become even closer in frequency. This is consistent with the standing wave model employed and also implies that the polarization dependence of the ERs in Figure 3.1 is due to the non-uniform width of the rings.

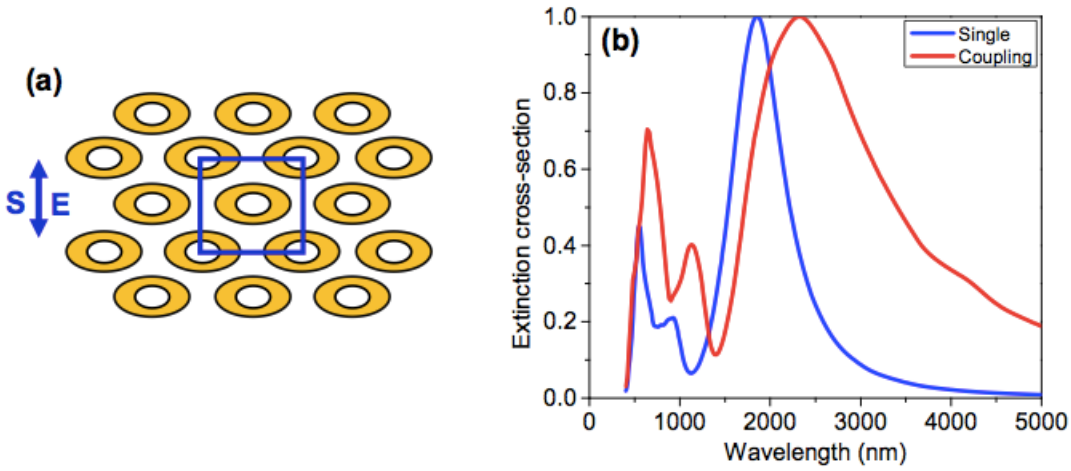

Figure 3.4 : A theoretical simulation showing the effect of coupling on the resonances of the ERs for AR = 1.84 for the S-polarization. (a) ER arrays used for simulation. (b) The theoretical extinction spectra of a single ER (blue line) and an ER array (red line) for the S-polarization. A clear red shift is observed for the array, which indicates the existence of a coupling effect for the S-polarization. The theoretical data were calculated using Lumerical FDTD. For these simulations, uniform meshing (2 nm) in all directions was applied and a Drude model was used to account for the gold material, which is the same as that used in the COMSOL simulations.

In order to further confirm that this red-shift was caused by the nonuniform ring width, we simulated the extinction spectra of ERs (AR = 1.84) of a uniform ring width of 50 nm. As expected, the spectra were almost polarization independent (Figure 3.3). Figure 3.2a also shows that l_L increases monotonously with increasing AR, which explains why λ_L red-shifts with increasing AR, as shown in Figure 3.1c. In contrast, l_S first decreases with increasing AR with a minimum for AR = 1.54, and then undergoes a monotonous increase for larger AR. This is consistent with the trend for the simulated λ_{S1} (Figure 3.1c), where the S1 resonance blue-shifted when the AR was increased from 1.0 to 1.54 and then red-shifted as the AR value was further increased. Again, both the standing wave model and the simulations were based on a single ER. As a result, this clearly explains the variation of dipolar resonances in the simulation. However, as noted above, the coupling between periodic ERs can also cause a red-shift of the resonance. To demonstrate this, we ran an additional simulation to compare the resonances of a single ER with a periodic ER array (Figure 3.4). As expected, the resonances for the ER array were red-shifted with respect to those for a single ER.

In order to further understand the resonances, we plotted the experimental resonance peaks (λ) as a function of l_{eff}/m (Figure 3.2b). As expected from eq 3.2, λ followed a linear relationship with l_{eff}/m. This agreement suggests that the generalized standing wave model can be used as a simple and quantitative description of the polarization dependent resonant peaks of the ERs. Moreover, the resonances

of the ERs could be simply predicted from the dimensions of the ERs, which is key for sensor design. Additionally, n_{eff} was derived from the slope of Figure 3.2b to be 1.123. As the gold ERs were surrounded by two media, the glass substrate and air with refractive indices of 1.47 and 1.00, respectively, this value is within a reasonable range.

3.3 Dark-Mode Plasmonic Resonances of ERs

3.3.1 Excited Dark mode of ERs at oblique incidence

As we discussed and predicted at the beginning of this chapter, dark-mode resonances of ERs could be excited at oblique incidence. In order to achieve oblique incidence, experimental methods were performed and Figure 3.5a illustrates different excitation geometries. As compared to normal incidence, oblique incidence has four incidence scenarios (LL, LS, SS, and SL) with the combination of two polarization directions (L and S) and two oblique incidences (L and S).

Figure 3.5b compares the extinction spectra from experiments of ERs-1.84 obtained at oblique incidence ($\theta = 20^\circ$ for top four spectra) with those at normal incidence ($\theta = 0^\circ$ for bottom two spectra). When the incidence angle is switched from normal to oblique, spectra of ERs are also polarization-dependent and four scenarios could be divided into two cases. In one case (SL and SS), the spectra are identical to the corresponding spectra at normal incidence (NL and NS), indicating that no dark-mode resonances are excited. In the other case (LL and LS), more resonance peaks

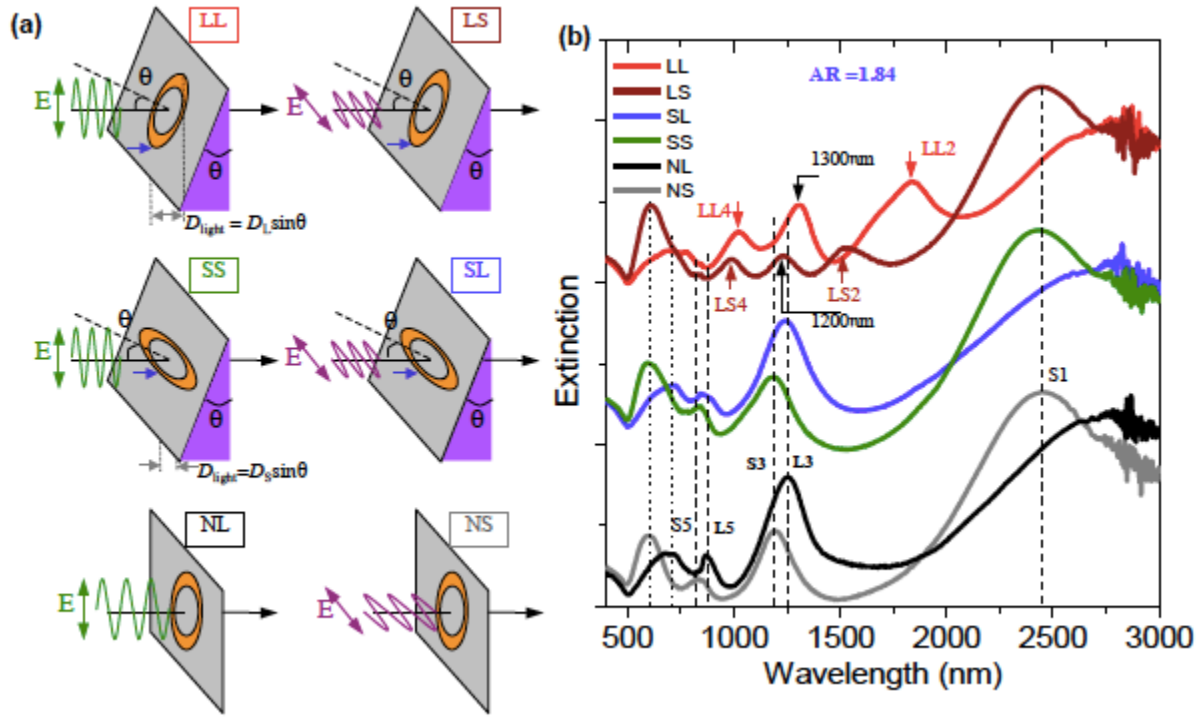

Figure 3.5 : (a) Schematic illustrations of four scenarios at oblique incidence (LL, LS, SS, and SL) and two scenarios at normal incidence (NL and NS) for the measurement of spectra. For the oblique incidence, the first letter (L or S) indicates that light wave reaches the near end of long (L) or short (S) axes of the elliptical ring first (shown as blue arrows) and the latter one indicates the polarization direction (L or S). θ is the incidence angle of light, which is identical to the angle of the wedge inserted under the sample. (b) Extinction spectra of elliptical rings with AR of 1.84 measured at six scenarios in (a). The incidence angle for all oblique incidences is 20°.

are observed as compared to the spectra at the normal incidence. We found that while the antibonding resonances maintain original wavelengths at normal incidence (two leftmost dot lines), some new symmetry-forbidden modes are excited between odd-mode resonances. In LS, S1 and S5 almost maintain original wavelengths and S3 slightly redshifts to 1200 nm. Clearly, two new peaks at 1561 nm and 996 nm are excited between odd-mode resonances. We labeled them as even mode resonances: LS2 ($m = 4$) and LS4 ($m = 4$). Similarly, in LL, L4 slightly red-shifts to 1300 nm two new even-mode peaks (LL2 for 1814 nm and LL4 for 1021 nm) are excited between odd-mode resonances. Here we also noticed that the shapes of the original odd-mode resonances are changed with the occurrence of new dark-mode resonances. For example, intensities of odd-mode resonances are reduced (L3 and S3) and even disappeared (L5 and S5) as incidence is switched from normal to oblique.

As demonstrated above, even-mode resonances are dark at normal incidence but become bright at oblique incidence. These even-mode resonances, forbidden at normal incidence, are also called dark-mode resonances. The appearance of dark-mode resonances could be attributed to a retardation effect, which results from the difference between the electric fields propagating from two different regions of the nanostructures. In case of normal incidence, the incident light wavefront reaches the perimeter of ring at the same time and therefore no dark-mode resonances are excited. In the case of oblique incidence, owing to the finite speed of light, the incident light wavefront reaches near end of long or short axes of ERs first (blue arrows pointing at

ERs), leading to the localized polarization charges at the near end. This explains the excitation of dark-mode resonances in LL and SL observed in Figure 3.5b.

Next, we'll explain why excitation of dark-mode resonances is dependent on the incident scenarios in this case (i.e., dark-mode resonances are excited only in LL and LS but not in SL and SS). Actually, the excitation of dark modes depends on the size of the nanostructure along the incident light. When the size of the nanostructure is small compared to the wavelength of incident light (λ_{light}), the electric field on each side of the nanostructure can be still assumed to be uniform and dark mode resonances will remain dark. However, when the size of the nanostructures is comparable to λ_{light}, dark-mode resonances will become bright and be excited in the spectra. For example, for nanoparticles, dark-mode resonances were found to excited when the size of nanoparticles was comparable to $\lambda_{light}/4$ because the electrical field in that case cannot be assumed to be uniform across the nanoparticles. In our case, the effective size of the ERs along the light wave direction, D_{light}, could be expressed as $D_{light} = D \cdot sin\theta (D = D_L or D_S)$ as shown in Figure 3.5a. Because $D_L > D_S$, the electrical field along the perimeter of the ERs is not uniform when the ERs were tilted along the long axis (LL an LS) but can be assumed to be almost uniform when the ERs were tilted along the short axis (SL and SS).

In order to theoretically confirm the occurrence of these dark mode resonances and the assignments of modes, we performed COMSOL simulations for ERs at different ϑ values (Figure 3.6). Figure 3.6 shows that the simulated extinction spectra of

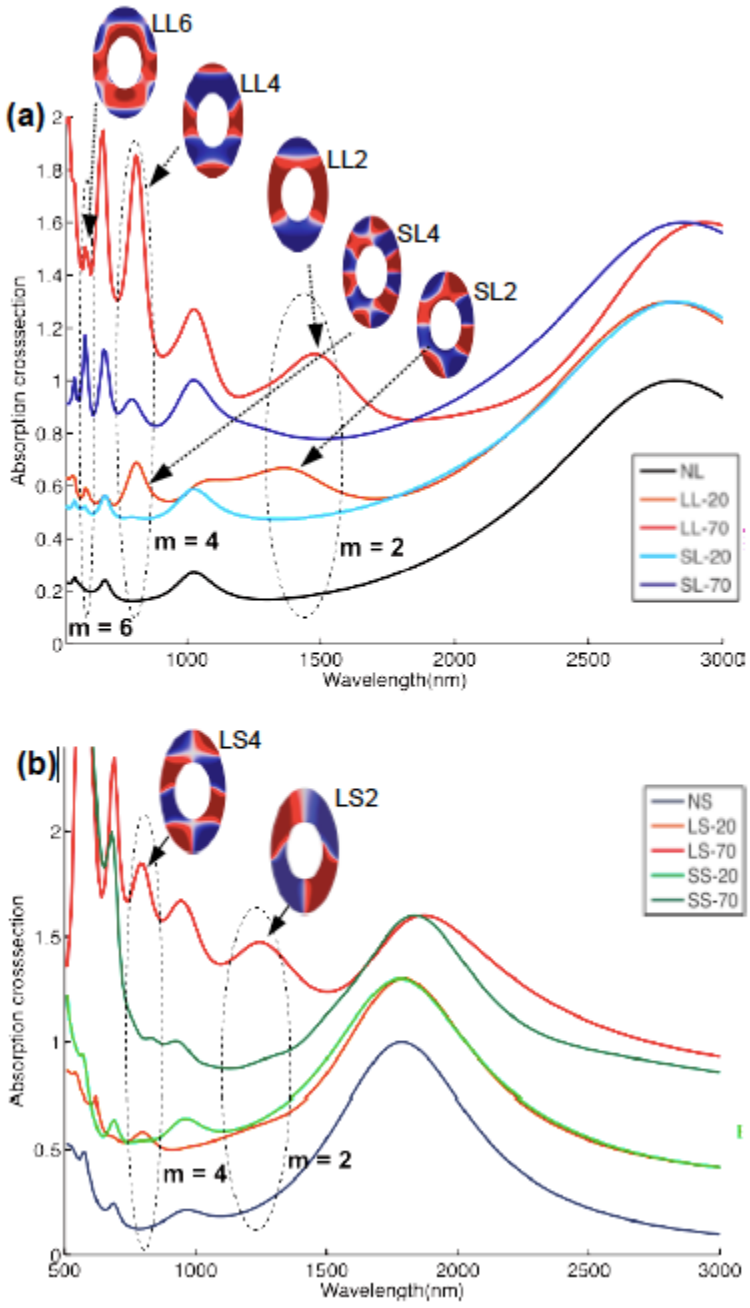

Figure 3.6 : Comsol simulation of the extinction spectra of ERs (AR = 1.84) at the incidence angles of 0°, 20° and 70° at (a) L-polarization (LL and SL) and (b) S-polarization (SL and SS). Insets are charge distributions of the corresponding dark-mode resonances.

ERs-1.84 at normal and oblique ($\theta = 20^\circ$ and 70°) incidences. The simulation spectra qualitatively reproduce the experimental data. The simulation spectra in L (Figure 3.6a) and S (Figure 3.6b) polarizations clearly show that only odd-mode resonances are excited at normal incidences (NL and NS). In LL and LS at the incidence angles of 20° and 70°, we noticed that all even-mode resonances ($m = 2$, 4, and 6) become bright. However, in SL and SS, less even-mode resonances are excited as compared to LL and LS. Mode-2 resonances are not visible in all four cases (SL-20, SL-70, SS-20, and SS-70). At a lower incidence angle of 20° (SL-20 and SS-20), no even-mode resonances are excited. At a higher incidence angle of 70° (SL-70 and SS-70), some of higher order even-mode ($m = 4$ and 6) resonances start to be visible but lower order even-mode ($m = 2$) resonances still remains dark. This trend clearly demonstrates that higher incidence angle promote the excitation of dark-mode resonances. In addition, in order to further confirm the assignments of dark modes, the corresponding calculated charge distributions of the excited dark-mode resonances are shown in the insets of Figure 3.6. Here the mode number (m) could be calculated to be half of node numbers in the charge distribution. In LL, the peaks at 1360, 810, and 620 nm are quadrupolar (m =2), octupolar ($m = 4$), and hexadecapolar ($m = 6$) plasmon resonances, as they exhibit 4, 8, and 12 nodes in the charge distributions, respectively (Figure 3.6a). In SL, the peaks at 790 and 620 nm have octupolar ($m = 4$) and hexadecapolar ($m = 6$) plasmon resonances with 8 and 12 nodes in charge distributions (Figure 3.6a). In LS, the peaks at 1240 and 790 nm have quadrupolar ($m = 2$) and

octupolar ($m = 4$) plasmon resonances with 4 and 8 nodes in charge distributions (Figure 3.6b).

3.3.2 Standing-wave model for dark modes of ERs

We have demonstrated that the reduced symmetry and retardation effects could excite all modes of resonances of ERs. Previous paper has shown that all odd-mode resonances increases with the increase of AR and can be fitted into a linear relationship. In order to quantitatively interpret even-mode resonances, we measured the spectra of all ERs in LL and LS at $\theta = 20^\circ$ (Figure 3.7a). In this case, all mode resonances (m = 1, 2, 3, 4, and 5) are excited in both L and S polarizations. It is found that the wavelengths of the even-mode resonances redshift with the increase of AR and increase linearly with increasing AR (Figure 3.7a,b). Similarly, we fitted all resonances into a standing-wave model: [21]

$$\lambda_m = 2n_{eff}(\frac{l_{eff}}{m}) - \lambda_0 \tag{3.5}$$

where l_{eff} is the effective length of the structure in the polarization direction, λ_m is the resonance wavelength, λ_0 depends only on the geometric structure, and n_{eff} is the effective refractive index. Here, l_{eff} in L (l_L) and S (l_S) polarizations can be calculated based on following equations:

$$l_L = (\pi/4)\sqrt{2(D_L^2 + (D_S - 2w_S)^2) - (D_L - (D_S - 2w_S)^2)^2/2} \tag{3.6}$$

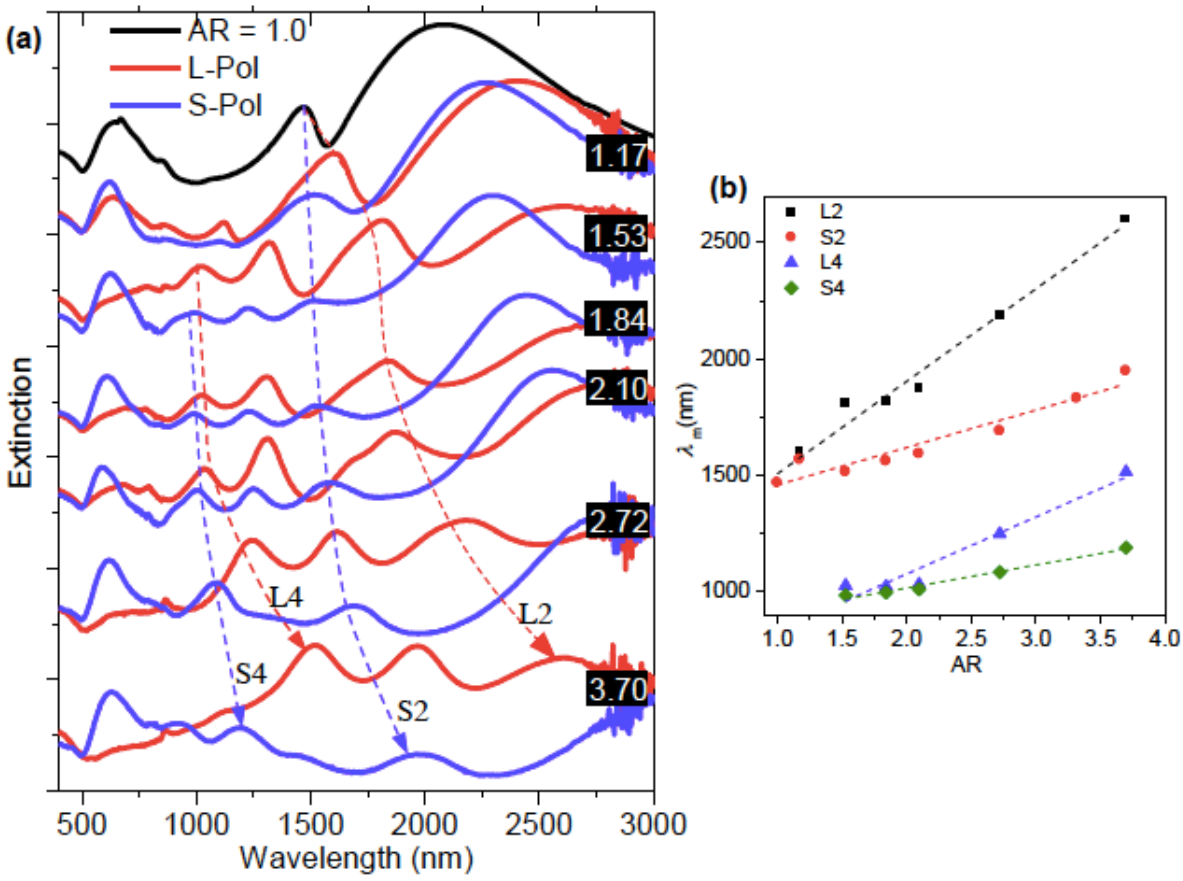

Figure 3.7 : (a) Extinction spectra of the elliptical rings with ARs of 1.0 (black line), 1.17, 1.53, 1.84, 2.10, 2.72, and 3.70, respectively, measured in LL (red) and LS (blue) at an incidence angle of 20°. The dash lines show the redshift of the even-mode resonance peaks (L2, S2, L4, and S4) with increasing AR. (b) Plot of the wavelength, λ_m, of the even-mode resonances ($m = 2$ and 4) at two polarizations (S and L) as a function of AR. The dash lines indicate the linear increase of λ_m with AR.

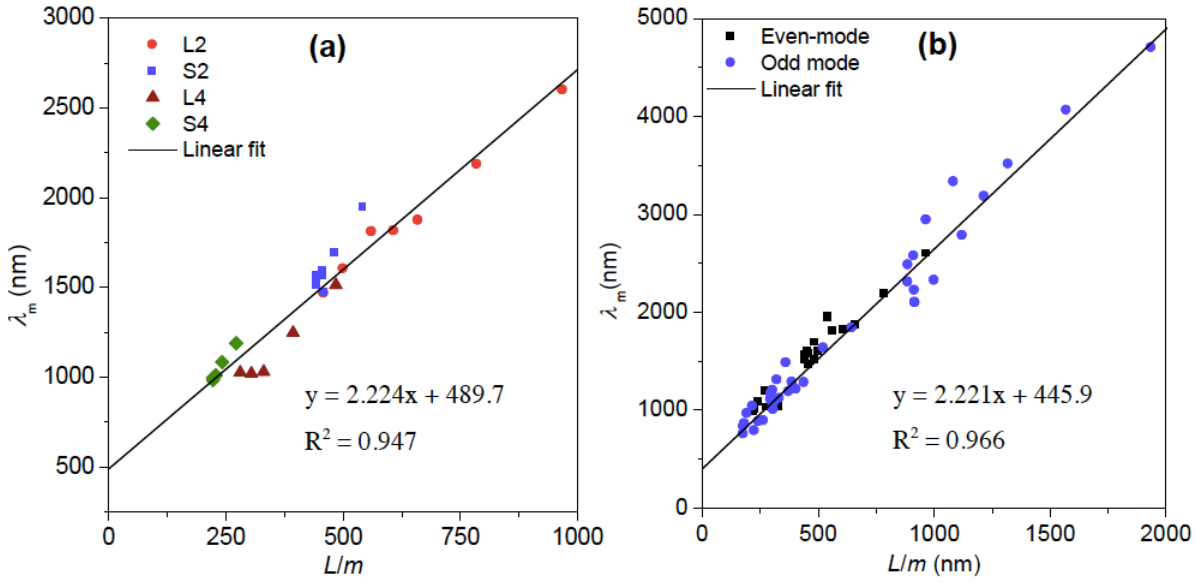

Figure 3.8 : (a) Plot of resonance wavelength, λ_m, as a function of l/m. (b) Plot of λ_m, of the odd- and even-mode resonances as a function of l/m. The straight lines are linear fits.

$$l_S = (\pi/4)\sqrt{2((D_L - 2w_L)^2 + D_S^2) - ((D_L - 2w_L) - D_S)^2/2} \tag{3.7}$$

We plotted λ_m as a function of (l_{eff}/m) in Figure 3.8a. Similar to the odd mode resonances observed above, even-mode resonances also have a linear relationship with (l_{eff}/m), resulting in a reasonable n_{eff} (1.112) between refractive indices of surrounding air ($n_{air} = 1.0$) and glass substrates ($n_{glass} \sim 1.47$). Moreover, we also found that both the odd- and even-mode resonance wavelengths could be combined and fitted into the linear standing wave model with a similar n_{eff} (˜1.111 in Figure 3.8b). Therefore, this universal linear expression allows us to predict both bright and dark resonances of ERs.

3.4 Fabrications of ERs

As an important part of tuning the plasmon resonances of the ERs, here I want to briefly introduce the fabrication methods of the ERs and the way we control the aspect ratio of the ERs.

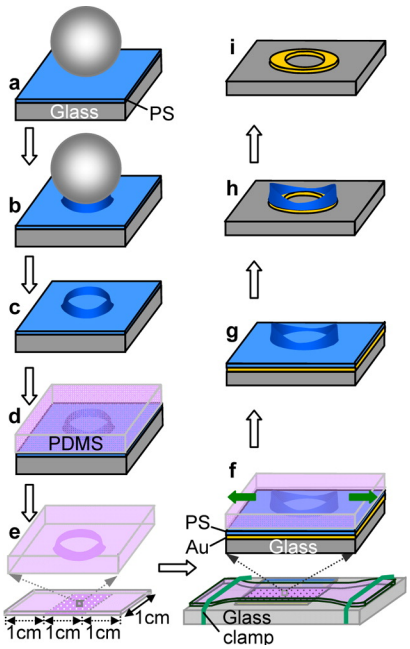

Figure 3.9 : Schematic procedure for fabricating gold ERs. (a) Depositing silica particles ($1\mu m$ in diameter) on an O_2 plasma treated PS film on glass ($\sim 1cm \times 1cm$). (b) Annealing the substrate above the T_g of PS. (c) Sonicating off silica particles. (d) Casting a PDMS film on the substrate surface followed by curing. (e) Releasing the PDMS film from the substrate and cutting the PDMS film into a rectangular sheet ($1cm \times 3cm$) with the patterned area in the middle (bottom panel). (f) Stretching the PDMS film and contacting it with a PS/Au/glass substrate and annealing at 130 °C for 10 min. The 3 cm long PDMS sheet, containing the patterned PDMS stamp in the middle, is used for stretching in order to make sure the aspect ratios of the stretched nanostructures are uniform in the middle (bottom panel). (g) Releasing the PDMS sheet to form elliptical PS rings. (h) Treating the substrate by RIE to remove the residual PS film and subsequent wet-etching of the uncovered portions of the Au film. (i) Removing the remaining PS by O_2 plasma treatment.

Figure 3.9 outlines the procedure for fabricating ERs. In this method, circular

polymer nanorings were fabricated using colloidal lithography analogous to previous investigations.[95] However, in previous work, the nanorings were not fabricated in ordered arrays because hydrophobic polystyrene (PS) films (water contact angle: $\sim 90^{\circ}$) were used as substrates for silica nanoparticle deposition and assembly. In order to obtain a hexagonally arrayed pattern, we modified the previous procedure slightly. Specifically, before depositing silica spheres, the PS film (molecular weight: $M_w \sim 97400$; thickness: $\sim 100nm$) was treated with an O_2 plasma for ~30 s, which rendered the surface hydrophilic (water contact angle: $\sim 0^{\circ}$). The short period of plasma treatment reduced the film thickness by ~40 nm but had no discernible effect on the subsequent capillary rise of PS along the silica spheres. The singular noticeable change was the formation of large-scale, well-ordered arrays.

To form an array of nanoparticles, a 20 μL aqueous droplet containing 2.0 wt % of 1 μm silica particles was spread onto the O_2 plasma-treated PS film and spontaneously formed an ordered array upon drying (Figure 3.9a). Since only the bottom layer of particles was responsible for the formation of patterns in the PS substrate, particle deposition was controlled to be somewhat thicker than one monolayer to ensure that the PS film was totally covered by silica spheres. The sample was then annealed above the glass transition temperature (T_g ~100 °C) of the PS film (T = 130 °C) for 10 min, leading to the formation of circular rings along the contours of the colloidal spheres (Figure 3.9b). After the silica particles were removed by sonication in a 1:1 volume mixture of water and ethanol, circular impressions were left behind in the

PS film (Figure 3.9c). These structures were used to create a PDMS stamp with annular apertures (Figure 3.9d). The PDMS mold was then removed (Figure 3.9e) and stretched by applying a uniaxial strain. Next, the strained elastomer was placed into contact with an unpatterned PS film on a Au coated planar glass slide (∼50 nm PS/50 nm Au/5 nm chromium/glass) (Figure 3.9f).

In order to facilitate conformal contact between the stretched PDMS sheet and the PS film, the thickness of the PDMS mold was kept to ∼1 mm. Upon annealing the sample at 130 °C for 20 min, PS filled into the cavities of the stretched mold by capillary forces (Figure 3.9f). At this point, the PDMS sheet was released from the substrate, leaving behind elliptical ring patterns (Figure 3.9g). To transfer this pattern to an underlying Au layer, the sample was treated by reactive ion etching (RIE) to remove the residual PS film and subsequent wet chemical etching to remove the exposed portions of the Au layer (Figure 3.9h). Finally, the remaining PS was removed by O_2 plasma treatment (∼3 min), leading to the formation of Au ERs on the glass substrate (Figure 3.9i).

Figure 3.10a shows an SEM image of circular PS rings obtained after annealing silica particles on a PS film at 130 °C for 10 min. The silica particles were removed before imaging. The hexagonal PS ring array was well ordered over macroscopic areas ($\sim 1cm \times 1cm$). The PDMS stamp replicated from the circular PS rings exhibited depressed circular apertures, as seen by AFM (Figure 2.10b). When the PDMS stamp was stretched under a 40% strain (i.e., an elongation of 40%), the circular

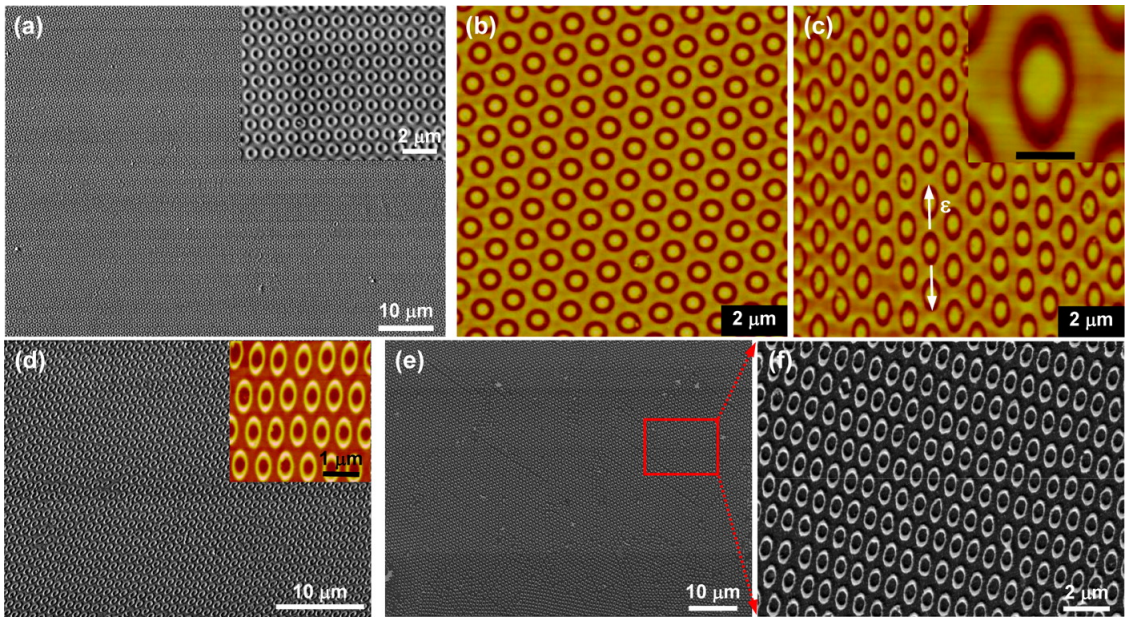

Figure 3.10 : (a) SEM image of circular PS rings. The inset is a high-resolution image. (b and c) AFM images ($10\mu m \times 10\mu m$) of the PDMS sheet replicated from circular PS rings before and after stretching, respectively. The high-resolution inset image in part c (scale bar: 500 nm) shows that the width of the aperture along the long axis is larger than that along the short axis. The white arrows indicate the strain direction. (d) PS ERs generated by using the stretched PDMS sheet as a mold. The inset is an AFM image ($5\mu m \times 5\mu m$) of the PS ERs. (e) SEM image of Au ERs on a glass substrate. (f) High resolution SEM images of part e.

apertures were transformed into ellipses (Figure 3.10c). The SEM image in Figure 3.10d demonstrated that elliptical PS rings could be generated successfully by using the stretched PDMS stamp as a template. The inset in this figure is an AFM image of the same substrate. After O_2 RIE and subsequent wet etching, highly ordered arrays of Au elliptical rings were formed on the glass substrate, as shown over a large area (Figure 3.10e) and close-up SEM image (Figure 3.10f).

The method described in Figures 3.9 and 3.10 can be tuned over a wide range of geometries by varying the parameters of the experiment. First, by using silica particles with a fixed size, varying the annealing time, temperature, conditions of RIE, and chemical wet etching could be exploited to control the diameter and width of the circular rings[14, 54] and hence the corresponding widths of the ERs. Of course, the size, inter-ring distance, and periodicity of the ER elements can also be tuned by changing the size of the silica particles. It should be noted that, once a PDMS stamp with circular apertures is fabricated (Figure 3.9d), it can be employed to create ERs of varying aspect ratios by tuning the applied strain. Moreover, a single PDMS mold can be used repeatedly. To demonstrate this, we used the mold from Figure 3.10b to generate all of the ERs described below.

Figure 3.11a shows that Au ERs with different aspect ratios (ARs) could be generated by simply applying varying strains (ε) to a single PDMS stamp. The AR of Au ERs is defined by the ratio of the outer diameter along the long axis (D_L) to that along the short axis (D_S) (schematic diagram in Figure 3.11a). Without applied

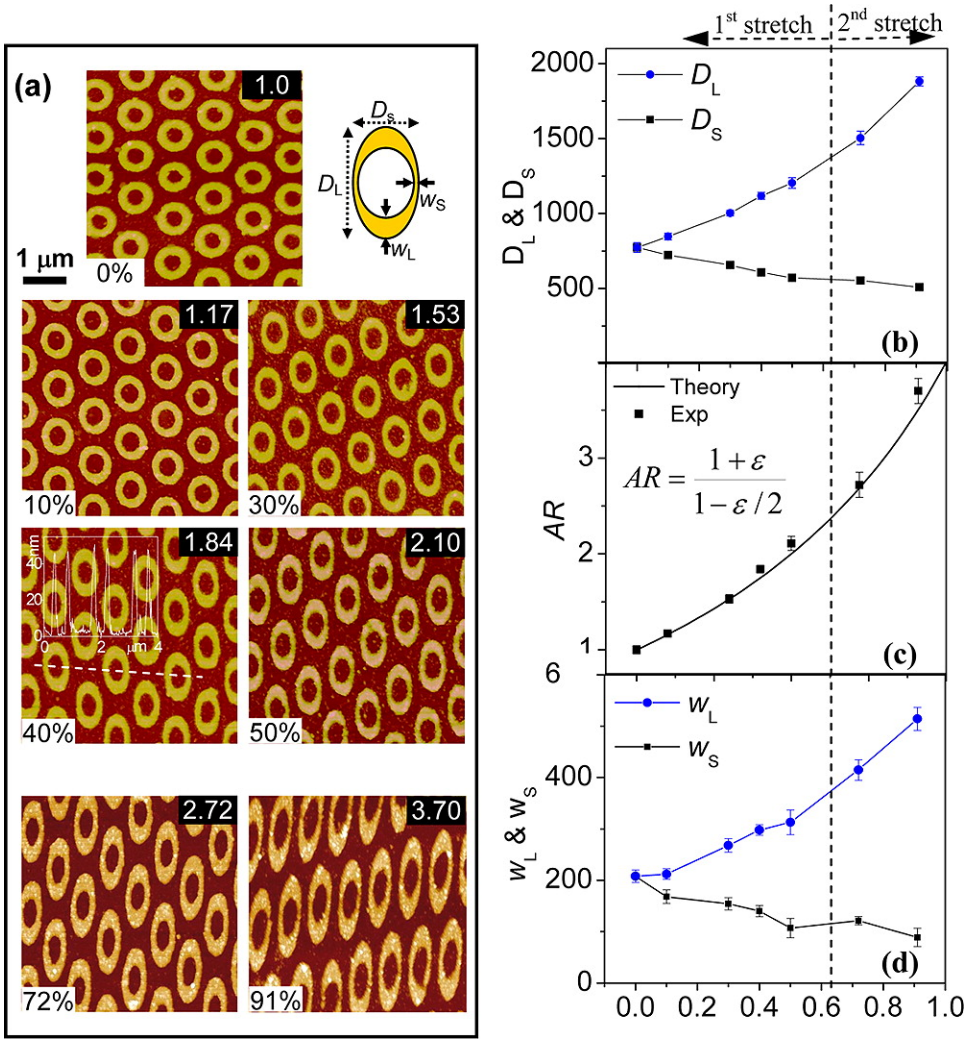

Figure 3.11 : Control of the aspect ratios (ARs) of gold ERs. (a) AFM images ($5\mu m \times 5\mu m$) of the gold ERs with different ARs (1.0, 1.17, 1.53, 1.84, 2.11, 2.72, and 3.70). The first five images were generated under strains of 0, 10, 30, 40, and 50%, and the bottom two were generated by using second-generation PDMS stamps replicated from the PS ERs with an AR of ∼1.84. Scale bar: $1\mu m$. The schematic diagram shows the parameters of the ERs. The line profile for an AR of 1.84 shows that the height of the Au structures is ∼45 nm. (b–d) Plots of the outer diameters (D_L and D_S), AR values of Au ERs, and widths (w_L and w_S), respectively, as a function of ε. The solid line in part c is the theoretic fit to the inset equations. The dashed line across the plots (b–d) is used to show that the data points to the left (right) side are obtained from the first (second) stretch.

strain, circular rings (AR = 1.0) were produced. As ε increased from 10, 30, 40, to 50%, the AR increased from 1.17, 1.53, 1.84, to 2.10, respectively. The maximum strain that could be applied on the PDMS sheet (i.e., the maximum elongation of PDMS at the breaking point) was ∼50%. This is smaller than the values that have been reported previously.[25, 109] The difference is that the present PDMS stamp is stretched and held in place at 130 °C instead of room temperature. Generally, the elongation of PDMS at its breaking point decreases with increasing temperature.[109]

One strategy to further increase the AR could involve lowering the annealing temperature by using a lower molecular weight polymer (i.e., decreasing T_g). Herein, a secondgeneration PDMS stamp was employed instead.[102] To do this, ERs in PS with AR ∼ 1.8 were used as masters and applied to a new PDMS mold. Thus, the new unstretched PDMS template contained elliptical apertures with AR ∼ 1.8, and after stretching along the direction of the long axis, elliptical apertures with greater ARs were generated. The bottom two AFM images in Figure 3.11a show Au ERs with ARs of 2.72 and 3.70 that were formed by applying a strain of ∼30 and ∼50%, respectively, to the second-generation stamp. An iterative process could be employed if even higher aspect ratios were desired.

The increase of AR is the result of increasing D_L while decreasing D_S as a function of strain, ε (Figure 3.11b). Here, ε is defined as $\varepsilon = [(D - D_0)/D_0] \times 100\%$, where D_0 and D are the diameters of the apertures in the PDMS sheet before and after applying the stain, respectively. Note that D can be used for either D_L or D_S. When a stain,

ε, is applied to a templated PDMS sheet, the initial diameter, D_0, of the circular aperture along the direction of the applied strain increases to $D_L = (1+\varepsilon)D_0$. On the other hand, D_S is reduced to $D_S = (1-v\varepsilon)D_0$. This later shrinkage is caused by a Poisson contraction[26]of PDMS, and v is the Poisson ratio of PDMS ($\sim$0.5). As a result, the AR of the elliptical apertures (Figure 3.11c) can be written as

$$AR = \frac{1+\varepsilon}{1-\varepsilon/2} \tag{3.8}$$

which can also be approximated as the AR of the resulting Au ERs. For the second-generation PDMS stamp, the resulting AR should be

$$AR = \frac{1+\varepsilon_1}{1-\varepsilon_1/2} \cdot \frac{1+\varepsilon_2}{1-\varepsilon_2/2} \tag{3.9}$$

where ε_1 and ε_2 are the stains applied in the first and second rounds of the stretching processes, respectively. Inserting the values of ε_1 and ε_2 into eq 3.9 results in theoretical ARs of 2.68 and 3.50 after second generation stretching (bottom two images in Figure 3.11a). This agrees resonably well with the measured values ($\sim$2.72 and $\sim$3.70). For simplicity, the Au ERs generated by using second-generation PDMS stamps can be considered to be generated by a one-time stretching under an effective strain (ε_{eff}):

$$\frac{1+\varepsilon_1}{1-\varepsilon_1/2} \cdot \frac{1+\varepsilon_2}{1-\varepsilon_2/2} = \frac{1+\varepsilon_{eff}}{1-\varepsilon_{eff}/2} \tag{3.10}$$

For the ARs of 2.72 and 3.70, ε_{eff} is ∼72 and ∼91%, respectively. Plotting a theoretical curve from the calculated AR due to the strain shows that all the experimental values agree well with this model (Figure 3.11c).

It can be readily observed that the ring width of the ERs is not uniform along the perimeter of the ERs. Indeed, the width reaches a minimum, w_S, normal to the stretching direction and a maximum, w_L, parallel to it (schematic diagram, Figure 3.11a). This width difference, which results at the PS templating step, is caused by strain-induced elogation/contraction of the long/ short axes. While the apertures at the long axis are stretched, those at the short axis are compressed due to Poisson contraction. This leads to much of the width difference. Moreover, the inner PDMS circles are unattached from the larger matrix being stretched. As such, they deform less than the surrounding region, which further increases the difference between w_L and w_S. The resulting width of the Au ERs can be tuned by several processes, including capillary filling by the PS film, O_2 RIE, and wet etching. Since all the lithographic conditions were kept constant as the strain was increased, w_L and w_S also increased and decreased, respectively, with ε in the present case (Figure 3.11d).

3.5 Summaries and Conclusions

In summary, we have demonstrated a simple patterning technique based on colloidal lithography to fabricate well-ordered PS and Au ERs over large areas ($\sim 1cm^2$ in this paper) in a highly controlled manner. One unique advantage of this method

was that it enabled the scalable fabrication of Au ERs with varying AR by simply tuning the strain. This previously required using different molds in soft lithography or employing EBL. Due to the ability to control the aspect ratio of the rings and therefore the plasmonic resonance positions in experiments, our method provides an effective platform for LSPR sensor design in a wavelength range from the optical to the infrared. Additional applications of these structures may involve optical coatings and filters. In fact, some extinction resonances are quite narrow and can be tuned to block incident light at specific wavelengths.

Moreover, we have demonstrated experimentally and theoretically that elliptical gold nanorings exhibited multiple plasmonic resonances. While only odd-mode resonances are visible at normal incidence, both odd- and even-mode resonances become visible at oblique incidence. The excitation of even-mode or dark-mode resonances is not only dependent on the incidence angle but also on the size and aspect ratio of ERs. Exeprimental and simulation data indicate that the excitation of dark-mode resonances is the result of the phase retardation. We also show that the intensities of the plasmonic resonances varies with the incidence angle. Moreover, a standing-waving model to quantitatively analyze all multiple resonances, which provided a simple designing guideline for the potential application of these structures to sensors and diagnosis.

Chapter 4

Angle- and Spectral-Dependent Light Scattering from Plasmonic Nanocups

4.1 Introduction

Plasmons, the collective electronic oscillations of metallic nanoparticles and nanostructures, are at the forefront of the development of nanoscale optics. The sensitivity of the properties of plasmonic nanoparticles to geometry, dielectric environment, and light polarization permits many degrees of freedom in the design of plasmonic structures for specific phenomena or applications. Excitation of the surface plasmons of metallic and metallodielectric nanoparticles generates intense, localized electromagnetic fields that enable processes such as surface enhanced chemical spectroscopies.[24, 41, 65] Controlling the precise geometry and composition of individual[76, 82, 115] or collective arrangements[43, 93] of plasmonic nanoparticles easily tunes the excitation energy of these oscillations through the visible and near-infrared regions of the electromagnetic spectrum for various applications. Plasmonic nanostructures can also serve to couple optical signals to planar devices, enhancing the performance of light emitting diodes,[81] photodetectors,[18, 113] and solar cells.[6, 17] Learning how to design plasmonic structures for these applications requires a comprehensive understanding of how this class of nanostructures alter the light-scattering properties of planar substrates, and, conversely, how planar

substrates, as symmetry-breaking elements, alter the optical response of plasmonic nanostructures.[7, 22, 23, 44, 78, 89, 97]

Reduced-symmetry 3D nanostructures such as nanocups (also known as semishells), possessing both electric and magnetic plasmon modes, are important model systems for the study of the light scattering properties of nanoparticles on planar substrates. Nanocups consist of a hemispherical shell of metal fabricated around a dielectric nanoparticle core, and have been of increasing interest in recent studies of plasmonic nanostructures due to their unusual and unique light-scattering properties. [29, 69, 112, 111] Nanocups possess both an electric, axial plasmon mode and a magnetic, transverse plasmon mode at two distinct and easily discernable resonant frequencies.[29] These two plasmon modes have been shown to possess distinct and very different light-scattering characteristics.[69] The axial mode scatters light with the $cos^2\theta$ angular dependence of a dipole scattering source, while the transverse plasmon mode exhibits a unique light-bending property where incident light from a broad cone of input angles is scattered in a direction normal to the cup rim. [20, 30, 62, 69, 116] This new degree of freedom, not available in symmetric nanoparticles, is of particular interest for the coupling of light from free space into planar or other reduced-dimensionality structures.

We directly examine the angle-dependent light-scattering properties of nanocups on a planar substrate. To compare the light-scattering properties of these structures directly with those of the equivalent, fully spherical core shell nanoparticles on the

same type of substrate, we fabricate our nanocup structures directly from chemically synthesized nanoshells. The scattering from a submonolayer of oriented nanocups demonstrates the ability of these structures to scatter light preferentially out of the incident beam path. While previous studies associate light-bending behavior with the transverse plasmon mode of the nanocup, [69] here we observe that, in the presence of a substrate, the axial plasmon mode can also possess light-refractive properties. The sensitivity of the angular scattering profile to nanometer-scale geometric irregularities of the nanocup rim, characteristic of the reactive ion etching process applied to nanoshells, is also observed. We also find that small changes in the dielectric permittivity of the substrate local to the nanoparticle can result in sizable effects on its light-scattering properties. Simulations of the nanoparticle substrate system using the finite element method (FEM) allow us to deduce the physical origin of both spectral and angular shifts in the light-scattering properties observed in experiments

4.2 Results and Discussions

4.2.1 Nanoparticle Scattering Profiles

Extinction measurements of nanocups and nanoshells allow us to directly compare the plasmonic properties of the etched nanocups with the spherically symmetric nanoshells from which they were obtained (Fig. 4.1). Here the nanoshells were deposited on transparent glass substrates to facilitate the optical extinction measurements. The samples were placed at an angle of 45° with respect to the incident

light, and P-polarized incident light was used, to correspond to our light scattering measurements. The nanoshell has one principal dipolar plasmon mode (Fig. 4.1a). [76, 77, 98]Three-fold degeneracy, as illustrated by charge distributions, due to the symmetry of the nanoparticle, allows this dipole mode to be excited by both S- and P-polarized incident light (Fig. 4.1a inset). As expected, the orientation of the electric dipole moment of the plasmon mode is solely controlled by the incident direction and polarization of light. Under P-polarized light, the degeneracy has been shown to be partially lifted, where the energy of one mode is red-shifted by the presence of the dielectric substrate.[49, 106]

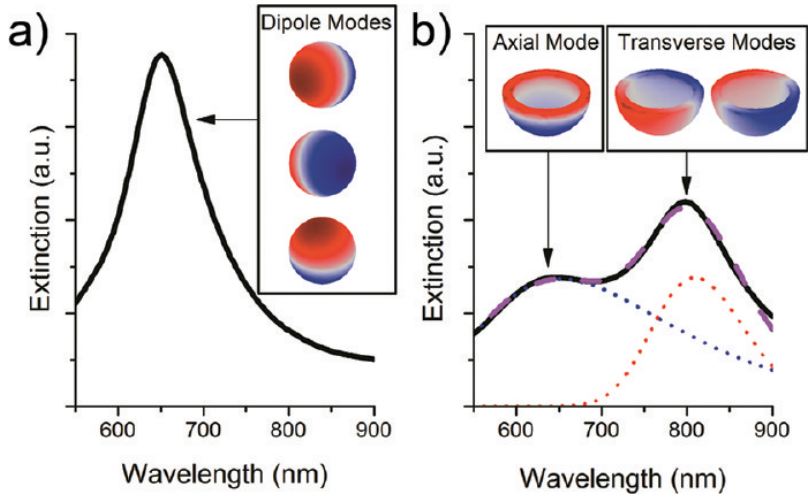

Figure 4.1 : Extinction measurements of nanoshells and nanocups on a glass substrate, oriented at 45°. P-polarized light excites the principal $l = 1$ dipole plasmon modes for (a) nanoshells and (b) nanocups. A two-peak Gaussian fit isolates the contribution of the axial mode (blue) and transverse mode (red) of the nanocup extinction spectrum of nanocups. Insets show simulated charge distributions obtained using FEM modeling, showing the qualitative orientation of the electric dipole for each plasmon mode in a homogeneous environment.

In contrast, the reduced symmetry of the etched nanocup creates two types of

orthogonal dipole plasmons with respect to the single axis of symmetry (Fig. 4.1b). The higher-energy, axial mode is centered at nominally 650 nm for the specific dimensions used in these experiments, and is characterized by charges oscillating along the axis of symmetry, from the rim to the bottom of the semishell. The two lower-energy, degenerate transverse modes are categorized as magnetic plasmon modes because charges oscillate from one side of the rim to the opposite side following the curvature of the metal.[29] Because the nanocup is an asymmetric particle, there is no axis of symmetry in the net electron motion and the net result is an optical frequency magnetic resonance. For the dimensions used here, the wavelength of these transverse modes varied between 800 and 850 nm between samples, due to the sensitivity to the etching process during fabrication. For this nanocup orientation, the axial mode is perpendicular to the substrate surface, while the two transverse modes are parallel to the substrate surface. An incident angle of 45° with respect to the surface normal was chosen to simultaneously excite both the axial and transverse modes of the nanocup: S-polarized light excites only one transverse mode, while P-polarized light excites both the axial and the other transverse mode. This geometry allows us to study the angular and spectral dependence of light scattered from both modes of the nanocup without varying the incident illumination angle.

Our angle- and wavelength-dependent measurements of nanoshells and nanocups on a glass substrate are shown in Figure 4.2. For a dipole nanoantenna in a homogeneous medium ($\varepsilon_{substrate} = 1$), with S-polarized incident light, this collection assembly

would measure a uniform intensity at all angles, due to the cylindrical symmetry of the dipole radiation pattern. P-polarized incident light would yield the expected $cos^2\theta$ intensity pattern, with maximum intensity along the axis of the incident light. The presence of a substrate ($\varepsilon_{substrate} > 1$) in the system imposes boundary conditions on the electromagnetic field at the interface. These conditions create a dark zone in the angular region close to the substrate where light cannot radiate into the far field, but instead refracts into the supporting substrate. [4, 63, 51] This property is observed for nanoshells on a glass ($\varepsilon_{substrate} = 2.5$) substrate for S-polarized incident light (Figure 4.2a). For P-polarized light incident on the same substrate-supported nanoshell sample, a dipolar scattering pattern is observed in the backscattered light (Figure 4.2b).

In contrast to symmetric nanoparticles, the reduced symmetry of the nanocup "locks" the orientation of the oscillating electric dipole with respect to the nanocup axis of symmetry. Incident light at 45° excites a combination of the two transverse modes or the single axial mode, allowing us to observe the angle-dependent light scattering from all plasmon modes of the nanoparticle, for different polarizations of the incident light. For S-polarized incident light, the electric field couples to the transverse nanocup mode oriented perpendicular to the reflection plane (Figure 4.2c). The measured intensity of the transverse mode, centered at 825 nm, is maximal at 0° with respect to the surface normal and falls to zero as the detector approaches the plane of the substrate. The majority of scattered light is radiated away from the

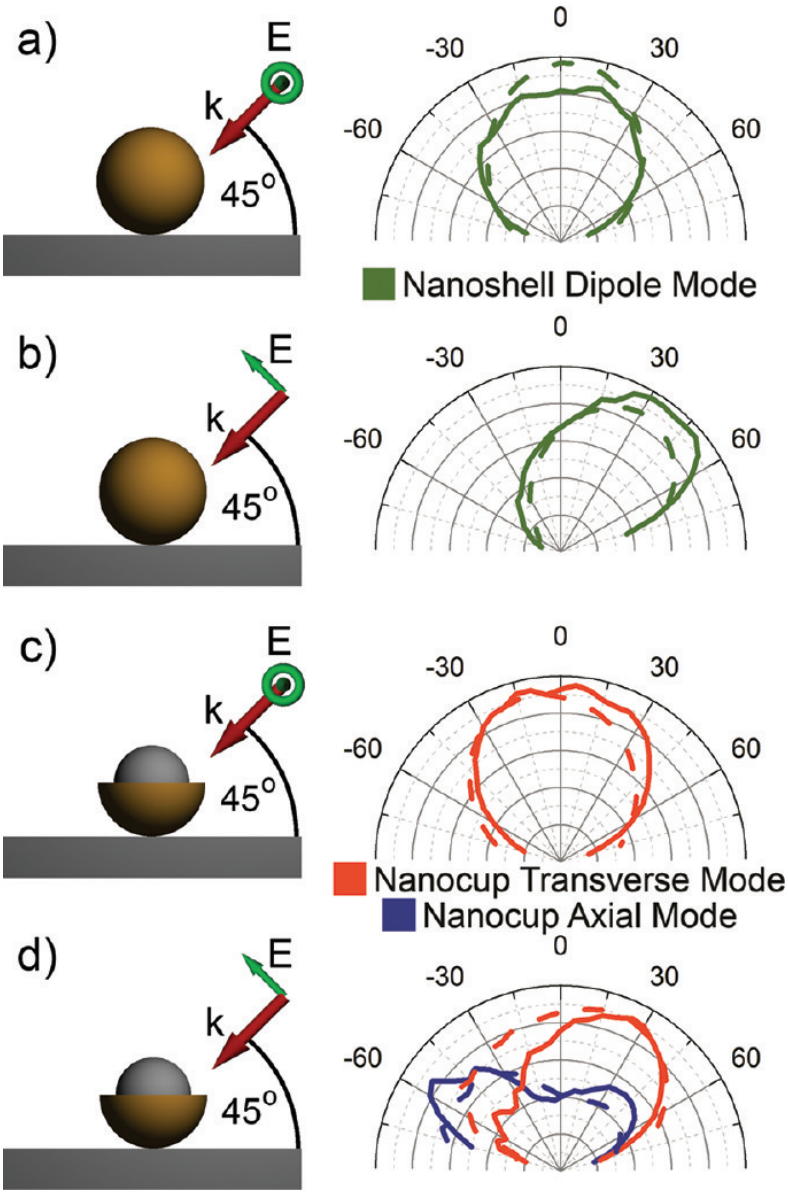

Figure 4.2 : Angular dependence of far-field scattering from nanoshell and nanocup plasmon modes on glass substrates. The amplitude of the Gaussian distribution for each mode is plotted as a function of detector position with respect to the surface normal (0°). Experimental (solid) and theoretical (dashed) data are plotted for the case of light incident at +45° with S- or P-polarization indicated by the inset schematics. (a) Scattering of S-polarized light by a nanoshell (λ = 650 nm). (b) Scattering of P-polarized by a nanoshell (λ = 650 nm). (c) Scattering of S-polarized light by an upright nanocup (λ = 850 nm). (d) P-polarized light incident on a nanocup excites both the transverse (λ = 850 nm) and the axial (λ = 675 nm) plasmon modes.

substrate or refracted into the substrate at an angle $\theta < \theta_c$, the critical angle for total internal reflection (TIR). A portion of the total energy radiated above, but also along, the interface couples into the substrate, as evident by the observation of the same dark zone discussed above.

For P-polarized incident light, a component of the incident field excites the transverse mode parallel to both the reflectance plane and the substrate surface. Simulations predict that this should result in light scattering normal to the substrate. However, in this case of the nanocups used here, the experimental scattering profile is slightly asymmetric but remains within the predicted envelope. The remaining component of the electric field, oriented normal to the surface, excites the axial nanocup mode. For this mode, the oscillating dipole is now oriented normal to the substrate and produces the expected dipole scattering pattern along the plane of the interface (Figure 4.2d). It is critical to note that this scattering is due to the nanocup geometry and not coupling to a high-dielectric substrate,[22, 23] as the dielectric constant of glass ($\varepsilon_{glass} = 2.5$) produces a weak image charge.

4.2.2 Effects of Nanocup Geometry

Examining the spectral dependence in addition to the angular dependence of scattered light from nanocups reveals more aspects of their mode-dependent far-field properties. Two-dimensional maps of both the wavelength (y-axis) and angle (x-axis) dependence of the scattered light from nanocups are shown in Figure 4.3. Experimen-

tal measurements of our samples yielded a two-dimensional map with both spectrally and angularly distinct scattering from the axial and transverse modes (Figure 4.3a). Theoretical simulations of this spectral and angular dependence show that in our experimental system, a red shift is preferentially observed for the transverse plasmon modes (Figure 4.3b). Such a red shift of the transverse mode cannot be caused by the interaction with the substrate because the axialmode is expected to exhibit amuch larger substrate-induced red shift than the transverse mode.[49, 106] To further investigate this red shift, we now examine how the detailed geometry of the nanocup rim influences its scattering properties.

Here we observe that the precise nanoscale geometry of the nanocup plays a significant role in determining the resonant wavelength of each plasmon mode. To more accurately simulate the experimental morphology of the etched nanocups, an oscillatory rim with the same thickness as the original gold layer was superimposed on the simple nanocup. The addition of this wavering edge geometry allows the collective oscillation of electrons in the transverse plasmon to produce higher charge densities in the sharp features of the new rim (Figure 4.3c). This increases the polarizability of the transverse modes, red-shifting them by approximately 50 nm, closer to the experimentally observed values. Because the charges at the circular rim would still remain evenly distributed with this new geometry, the axial mode does not shift appreciably due to this rim structure. The net effect of the change in geometry is an increase in the relative separation of the axial and transverse modes. The change in

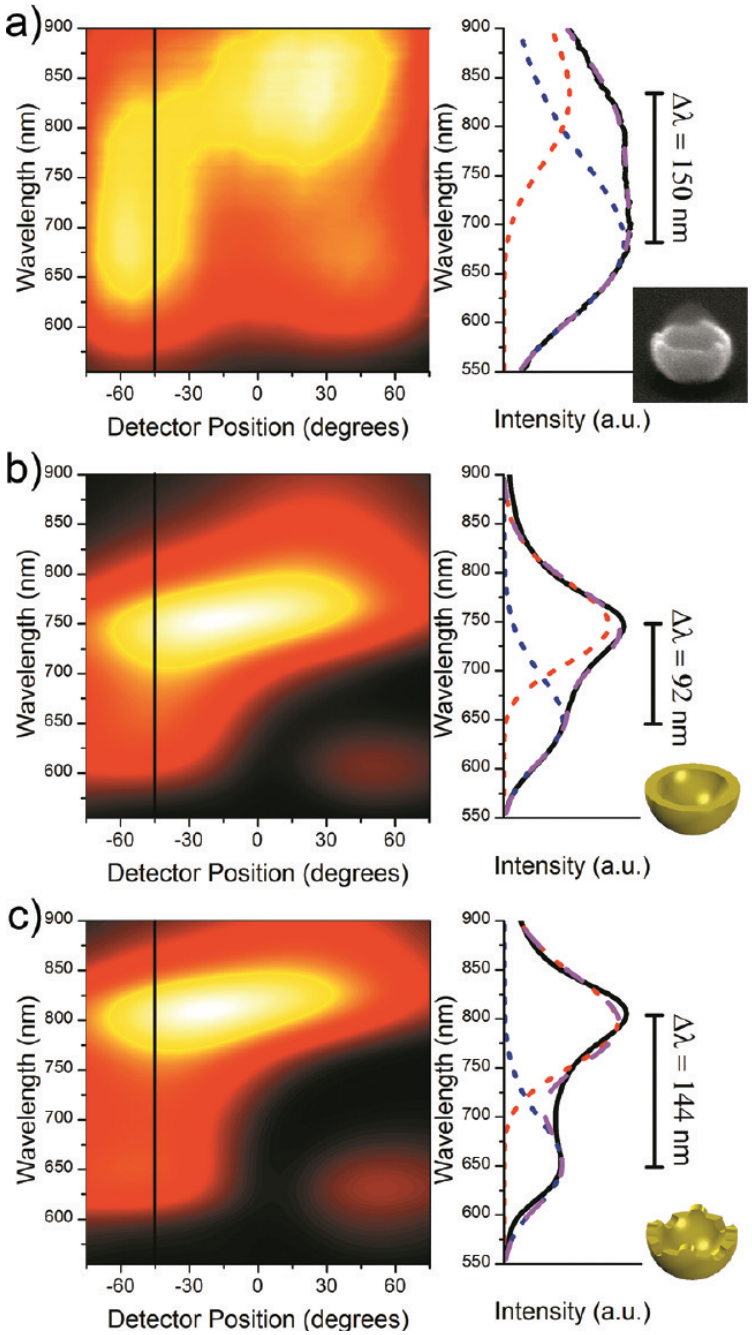

Figure 4.3 : Effect of nanocup geometry on plasmon mode energies. (a) Left: experimental scattering profile (color) of a nanocup on a glass substrate plotted as a function of detector position (x-axis) and wavelength (y-axis). Incident light was P-polarized and illuminated the sample from +45°. Right: plot of the scattered spectrum at −45° showing Gaussian peaks for the axial (blue) and transverse (red) modes. (b) Simulated smooth rim nanocup shows the same qualitative scattering features but reduced mode separation. (c) By adding an oscillatory rim to the simulated nanocup, the separation of the two nanocup modes increases by approximately 50 nm, similar to the experimentally measured mode separation.

rim geometry does not reorient the dipole moment of either plasmon mode, so the angular dependence of the scattering profile remains unaffected. Other minor deviations between theory and experiment are due to the ensemble-based measurement of the nanoparticles, which includes a random distribution of nanocups with these slight irregularities in the rim.

4.2.3 Effects of Substrate Permittivity

To further investigate the optical properties of a nanocup under the influence of a dielectric substrate, combined spectral and angular scattering measurements were performed for etched nanocups on a silicon substrate. Figure 4.4 presents the idealized case of nanocups deposited directly on a pristine, non-oxidized silicon substrate ($\varepsilon_{silicon} = 11.69$) and illuminated with P-polarized light (Figure 4.4a). Simulations predict an overall drop in scattering intensity (Figure 4.4b) relative to lower permittivity substrates, which is consistent with recent investigations of enhanced collection efficiency due to the deposition of plasmonic nanostructures on the input face of photodetectors and photovoltaic devices. [17, 96] The angular dependence of scattering (Figure 4.4c) is expected to be completely dominated by backscattering at the incident angle of illumination (+45°), mimicking the localized scattering behavior of P-polarized light on a spherically symmetric nanoshell. This profile is a consequence of strong coupling of the plasmon modes of a nanoparticle with the high permittivity substrate through interaction with its image charge.[49]

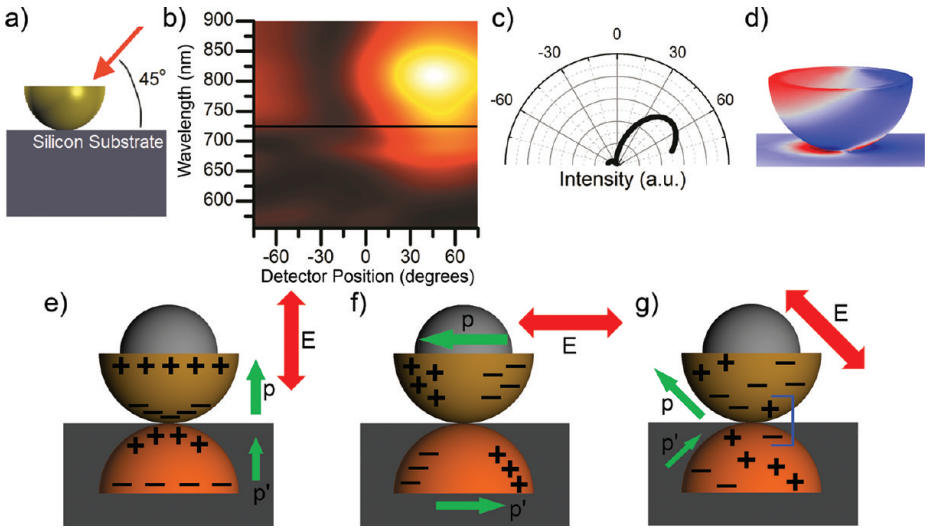

Figure 4.4 : Effects of a pristine silicon substrate on the plasmon spectrum and angular light scattering of a nanocup. (a) Schematic of nanocup/substrate simulation space with P-polarized light illuminating the sample from +45°. (b) Scattering profile (color intensity) of a nanocup on a silicon substrate plotted as a function of detector position (x-axis) and wavelength (y-axis). (c) In polar coordinates (degrees), the angular distribution of 725 nm scattered light is strongly localized in the direction of backscattering, dictated by orientation of the charge distribution (d) on the nanocup. (e) Qualitative orientation of surface charge on the nanocup and the image charge within the substrate for purely axial [left], purely transverse [center], and the experimental [right] polarization of incident light. The green arrows depict the orientation of the effective dipole moment of the nanocup, p, and the image charge distribution, p'.

In the image charge model, the magnitude of the image charge is modified by a factor proportional to $(\varepsilon - 1)/(\varepsilon + 1)$, which approaches unity for high-dielectric materials, such as silicon. Interaction with this image charge is more prominent with the axial plasmon mode (Figure 4.4e, left) due to the charge distribution along the axis of symmetry, specifically, the proximity of the charges at the bottom of the nanocup and the image charge projected on the surface of the substrate. The image dipole is aligned with the nanoparticle dipole, resulting in a larger net dipole and increased coupling with the incident radiation. The transverse mode (Figure 4.4e, center) is weakly affected since charges localized on the rim of the nanocup are well separated from their image charges on the substrate. In this case, the image and nanoparticle dipoles are oppositely oriented, weakening the net dipole moment of the system. Thus, in the presence of highdielectric substrates, the energy of the axial plasmon mode is red-shifted toward the energy of the transverse plasmon mode, and the separation of the resonant wavelengths of each respective mode is greatly reduced (Figure 4.4b).

In the case of 45° incidence and P-polarized light, the combination of both of these complex interactions explains the predicted scattering profile for 725 nm light (Figure 4.4c) and can also give rise to higher order (n > 1) plasmon modes. The charge distribution on the nanocup (Figure 4.4d) indicates that the principle nanocup modes, now with similar plasmon energies, have hybridized to form a net dipole oriented along the polarization of the incident laser. The image dipole of the nanocup pro-

duces an inhomogeneous electric field in the near-field region of the nanocup, allowing hybridization with higher order plasmon modes, demonstrated by the appearance of a faint linear quadrupole with an axis of symmetry aligned with the polarization of incident light. As a result, the charge distribution has a net dipole moment oriented along the polarization of the incident electric field. The radiation from this dipole explains the strong localized scattering observed in the direction of incidence (+45°). While the resonant wavelength for this mode is located around 825 nm, the scattering profile at 725 nm exhibits the same features and permits comparison of this idealized system with the more advanced model described below.

When a nanoscale dielectric layer is incorporated into the basic model (Figure 4.5a), we observe marked differences in the angular scattering spectra of the nanoparticle which provides useful insight into the properties of our experimental system. The addition of this dielectric more accurately reflects our experimental system (Figure 4.5b) which includes both a nanoscale native oxide layer and a nanoscale polymer layer to facilitate adhesion of the nanoparticles to the substrate. The simulation space was altered by including a 2 nm layer with an effective dielectric constant of $\varepsilon_{film} = 2.50$ between the nanocup and underlying substrate. Compared to the case of pristine silicon, the presence of a low-dielectric layer slightly blue shifts the axial plasmon mode away from the transverse modes and back toward the original resonance at 675 nm on glass. The angular dependence, however, indicates an entirely new scattering pattern compared to that of pristine silicon (Figure 4,5c). The presence of

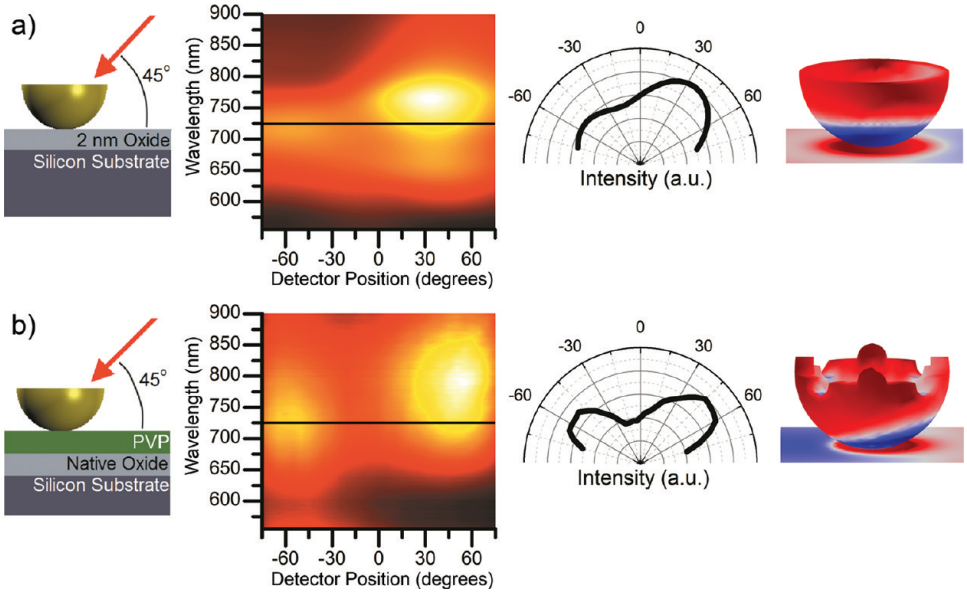

Figure 4.5 : Energy of the plasmon resonances in a symmetric silver heptamer Effects of a realistic silicon substrate on the plasmon spectrum and angular light scattering of a nanocup. In each panel is displayed (left to right): schematic of nanocup illumination and geometry of silicon substrate; scattering profile (color intensity) of a nanocup on a silicon substrate plotted as a function of detector position (x-axis) and wavelength (y-axis); angular distribution of 725 nm scattered light in polar coordinates (degrees); and charge distribution of the nanocup. In all cases, incident light is P-polarized and illuminates the sample from +45°. (a) Simulation: the addition of a 2 nm thick lowdielectric layer ($\varepsilon_{film} = 2.50$) atop the silicon substrate blue shifts the plasmon modes. A forward-scattering peak in the direction of specular reflection ($-45°$) begins to emerge in the angular scattering distribution. The charge distribution on the nanocup is now dominated by the axial mode. (b) Experiment: The native oxide/PVP layer on the silicon surface results in a blue-shifting of the plasmon modes and the emergence of both a forward and backward scattering lobe, consistent with simulations in (a). The (theoretical) charge distribution of a nanocup with an oscillatory rim retains its primarily axial mode character.

this low-dielectric barrier between the nanocup and the silicon creates two interfaces, deviating from the simple image charge model. Despite the extremely small thickness of the lowdielectric film, the effect on the scattering profile is significant in our experimental characterization of this system. While the strongest scattering remains primarily in the direction of incidence (+45°), there is now, in addition, a significant amplitude of forward scattering in the direction of specular reflection (−45°). This is facilitated by the original nanocup axial mode which completely dominates the transverse and quadrupolar contributions. This study shows that small, highly localized changes in the dielectric of an underlying substrate may have large effects on the light-scattering properties of nanocups, a property that may provide a useful route to active control of light-scattering properties.

4.3 Finite Element Method (FEM) Modeling.

All simulations were performed using the COMSOL 4.2 RF module (commercial FEM software). A spherical simulation space was surrounded with a perfectly matched layer (PML) to absorb scattered light and then a scattering boundary condition to prevent reflections. The space, including the PML regions, was divided by a plane to simulate the dielectric interface of the supporting substrate. The dielectric constant, εsubstrate, for the bottom hemisphere was chosen to reflect the appropriate substrate used in the experiment ($\varepsilon_{glass} = 2.50$, $\varepsilon_{silicon} = 12.69$), while the upper hemisphere was modeled as air, $\varepsilon_{air} = 1$. An effective oxide layer was modeled as a second

interface with a constant thickness and with a dielectric constant of $\varepsilon_{oxide} = 2.50$. The incident radiation was defined as a simple monochromatic plane wave incident at 45° that satisfied the Fresnel equations at the dielectric interface. This approach counters the major reflections between the interface and PML layers. The simulation space does not implement periodic boundary conditions, which represent a perfect array as opposed to the randomly oriented particles in the experiment.

A nanoshell was modeled as two concentric spheres of radius $[r_1, r_2] = [60, 78]$ nm at the center of the simulation space. The optical constants of the Au outer shell were described using experimental values [47] and the silica core as an isotropic dielectric with $\varepsilon_{core} = 2.04$. To model a simple nanocup, the upper half of the Au shell was removed, leaving a Au semishell with a smooth rim. A model created to more accurately simulate the structure of the fabricated nanocups involved adding and removing semicircular (radius 15 nm) patches of gold with the same thickness as the original shell to and from the smooth rim (Figure 4.6). This wavering edge is a representative geometry of the inhomogeneous rim that results from the plasma etching process. At the bottom of each particle, a 3 nm facet was created to properly model the curvature of the nanoparticle coming into contact with the flat substrate surface. For a reasonable approximation of the far-field radiation patterns, a near-field to far-field transformation was performed in postprocessing by performing on a well-defined surface around the nanoparticle. Because of the supporting substrate, the transformation surface is hemisphere exclusively above the interface. For each

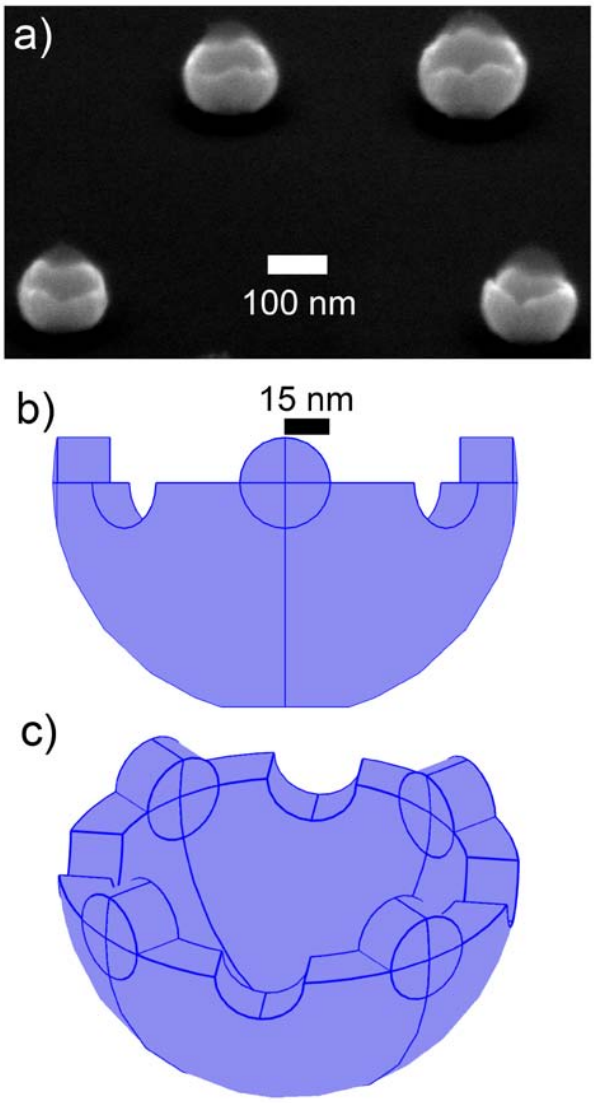

Figure 4.6 : Detailed geometry of wavering rim on experimental and simulated nanocups. (a) SEM micrographs of nanocups taken at an oblique angle of 70° reveal the rim morphology of the entire nanocup. (b) The geometry of the simulated nanocup mimics the inhomogeneous nature of the nanocup sample with a series of semi-circular (15 nm radius) bumps and depressions in the rim of half a nanoshell. (c) The two features are alternately positioned around the circumference of the rim in even increments to approximate the random variations of individual nanocups in the ensemble measurements.

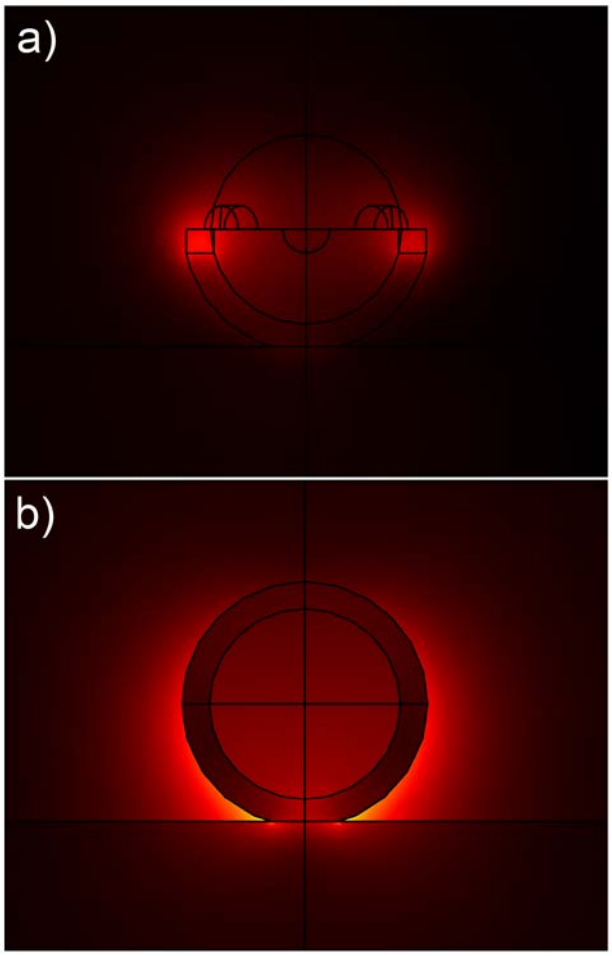

Figure 4.7 : Simulated scattered electric field magnitude around a nanocup and nanoshell. (a) The nanocup geometry allows for a higher degree of localization of the scattered electric field. The field intensity is reduced compared to a (b) nanoshell.

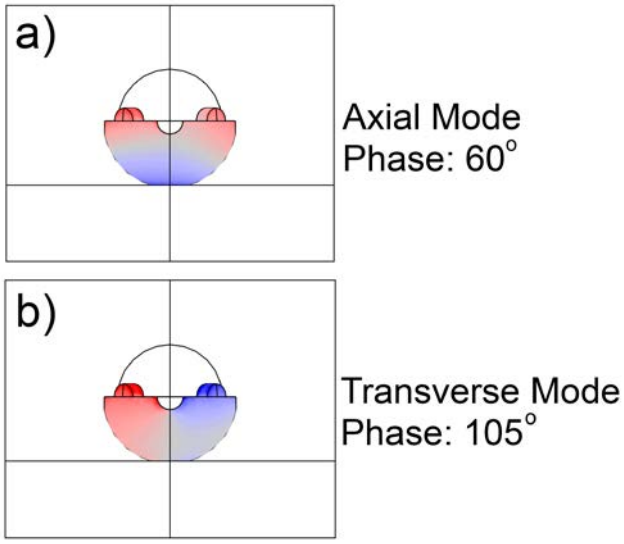

Figure 4.8 : Charge distribution on nanocup excited at 700 nm. In the region of spectral overlap, both the axial and transverse modes are excited by the same wavelength at different phases. The relative phase offset between (a) the nanocup axial mode and (b) the transverse mode is 45° and does not facilitate destructive interference.

detector position and simulated wavelength, the far-field intensity was integrated inside the angular region of this transform surface that corresponded to the collection cone of the optical assembly. Electric field plots (Figure 4.7) easily identify the localized field enhancements and plasmonic hot-spots. Charge plots were generated by applying Gauss's Theorem at the surface of the particle. The difference between the orthogonal component of the electric field immediately above and below the metal surface within an infinitely small pillbox was calculated to obtain the surface charge density. The phase of the incident wave was adjusted to find the maximumamplitude of the resonant charge oscillations of the plasmon modes (Figure 4.8).

4.4 Summaries and conclusions

In this chapter, we have examined the spectral- and angle-dependent light-scattering properties of plasmonic nanocups, through experimental studies and numerical simulations. The transverse and axial plasmon modes of a nanocup scatter light in distinct angular patterns that are sensitive to the presence of a dielectric substrate and its local permittivity adjacent to the nanoparticle. On low-dielectric substrates, both the axial and transverse nanocup modes scatter light in directions determined by nanocup orientation. With a high degree of sensitivity, the permittivity of the underlying substrate affects not only the wavelength of the resonances but also the angular light scattering of the system in significant ways. The different angular scattering and wavelength response from the axial and transverse nanocup modes make the nanocup an interesting particle for the nanoscale manipulation of light in three dimensions. The sensitivity of this system to geometric and environmental factors may present opportunities for active, substrate-mediated control of light scattering.

Chapter 5

Manipulating Magnetic Plasmon Propagation in Metallic Nanocluster Networks

5.1 Introduction

Plasmons of metallic nanostructures, despite being described by classical electromagnetic theory, exhibit characteristics analogous to the wave functions of atoms and molecules.[83] One of the simplest examples of this analogy is a dimer composed of two gold nanoparticles. When the two particles are brought into close proximity, their plasmons mix and hybridize, giving rise to the formation of bonding and antibonding plasmonic modes.[53] This interaction closely resembles the formation of molecular orbitals in a homonuclear diatomic molecule. Plasmon hybridization theory can also be used to analyze the modes of multicomponent plasmonic nanoclusters with more complex geometries.[62] For instance, a plasmonic heptamer, with the D_{6h} symmetry of a benzene molecule, has been shown to possess an intriguing Fano resonance due to the interference of its hybridized subradiant and super-radiant modes.[5, 35, 37, 42, 64]

Plasmonic circuitry based on metallic nanostructures is a promising potential component of semiconductor-based large-scale integrated circuits.[12, 105] Optical frequency signals can be coupled to and propagated along plasmonic structures, which are not subject to the free-space diffraction limit of light.[105] Maier et al. demon-

strated that an electric plasmon waveguide composed of gold nanoparticles in a linear chain can support subwavelength electric plasmon propagation.[13, 67] However, due to significant losses, electric plasmon propagation along such a chain is restricted to a few hundred nanometers at best. Recently, we have shown that magnetic plasmons can efficiently propagate along a conjugated heptamer chain with a much larger field decay length of several micrometers,[60] providing a practical strategy for plasmon-based signal propagation.

In this chapter we investigate the optical properties of two complex nanoparticle nanoclusters whose spatial geometries are analogues of the organic molecules chrysene and triphenylene. We demonstrate that these artificial plasmonic molecules can serve as building blocks for magnetic waveguiding networks with a variety of functionalities. We first present a plasmon steerer based on an artificial chrysene molecule (Figure 5.1a), which can direct magnetic plasmons around large-angle bends. We then discuss a plasmon Y-splitter based on an artificial triphenylene molecule (Figure 5.1b), which can transport magnetic plasmons along two separate optical paths. Both of these magnetic plasmon waveguides exhibit propagation lengths of more than two micrometers, showing superior performance compared to their electric plasmon counterparts. We further show that a plasmon Y-splitter can also serve as an interferometric device to switch magnetic plasmon propagation on and off. Depending on the number of heptamer units on each branch of the splitter, constructive or destructive interference of the magnetic plasmons can take place between the two

optical paths. Finally, we present a Mach-Zehnder interferometer composed of two consecutive Y-splitters, which can efficiently split and combine propagating magnetic plasmons. Our magnetic plasmon-based subwavelength waveguides will provide an important blueprint for designing a new generation of nanoscale photonic devices with potential applications in energy transport, data storage, near-field microscopy, and other nanometer-scale technologies.[59, 61, 68, 66, 70, 86]

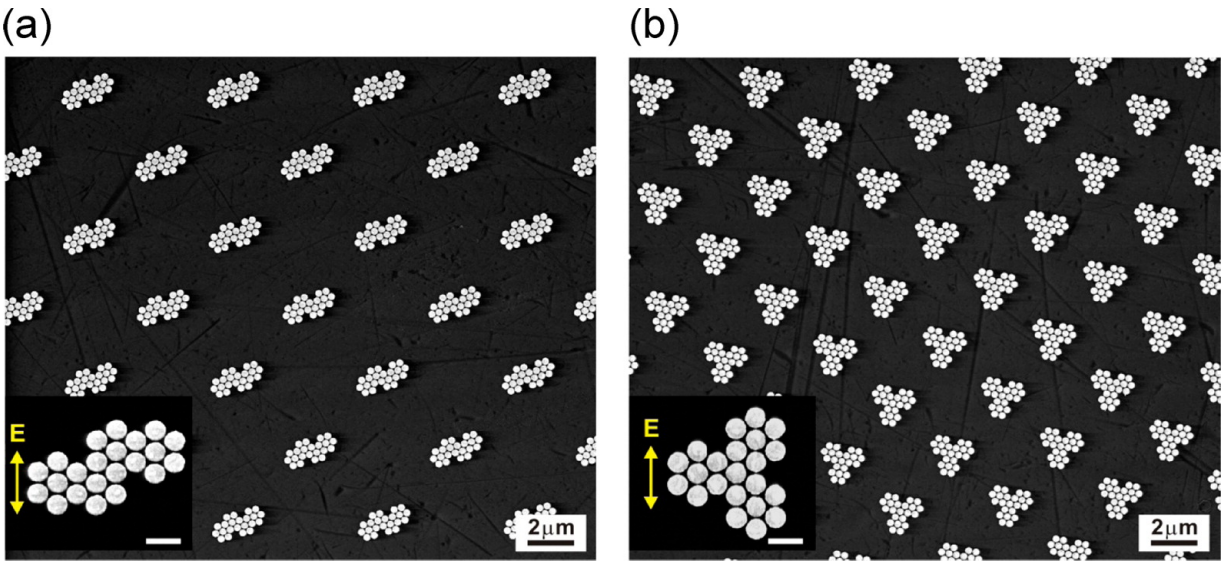

Figure 5.1 : ESEM images of an array of plasmonic chrysene structures (a) and plasmonic triphenylene structures (b) fabricated by electron-beam lithography. Insets: Enlarged views of individual structures with scale bars of 500 nm. The incident light polarization for spectral measurements is indicated in the insets.

5.2 Results and Discussions

Figure 5.1a and b present scanning electron microscopy images (ESEM, FEI Quanta 400) of the plasmonic chrysene and triphenylene structures, respectively. The structures were fabricated by electron-beam lithography on a quartz substrate using a pos-

itive resist (polymethyl methacrylate, PMMA). After development, a 2 nm chromium adhesion layer followed by an 80 nm layer of gold was evaporated onto the structures by electron-beam evaporation. Subsequently, the PMMA was removed by lift-off in N-methyl-2-pyrrolidone. Each sample consists of an array of structures covering an area of $80\mu m \times 80\mu m$. The periodicities in both directions for each structure are 2600 nm. The diameter and thickness of the gold particles are 260 and 80 nm, respectively, and the interparticle gap distance is 30 nm (Figure 5.1). The spacing between the unit cells does not lead to diffractive coupling in our spectral region of interest.

The optical properties of the samples were characterized using a Fourier-transform infrared spectrometer (FTIR, Bruker Vertex 80v) equipped with a microscope (Hyperion 3000). For excitation of the structures, we utilized linearly polarized light at normal incidence. The direction of polarization is indicated by the yellow arrows in the insets of Figure 5.1. The measured extinction (1-transmittance) spectrum of the plasmonic chrysene structure is shown in Figure 5.2a. There are two subradiant resonances that appear as minima at 1100 and 1500 nm within the broad spectral profile of the structure. In order to identify the spectral characteristics, simulations were performed using a commercial implementation of the finite element method (COMSOL Multiphysics). In the simulations, a single nanostructure was defined in the simulation window, and the extinction and absorption fields were solved. Perfectly matched layer and scattering boundary conditions were used to eliminate numerical artifacts at the simulation window boundary. The permittivity of the glass sub-

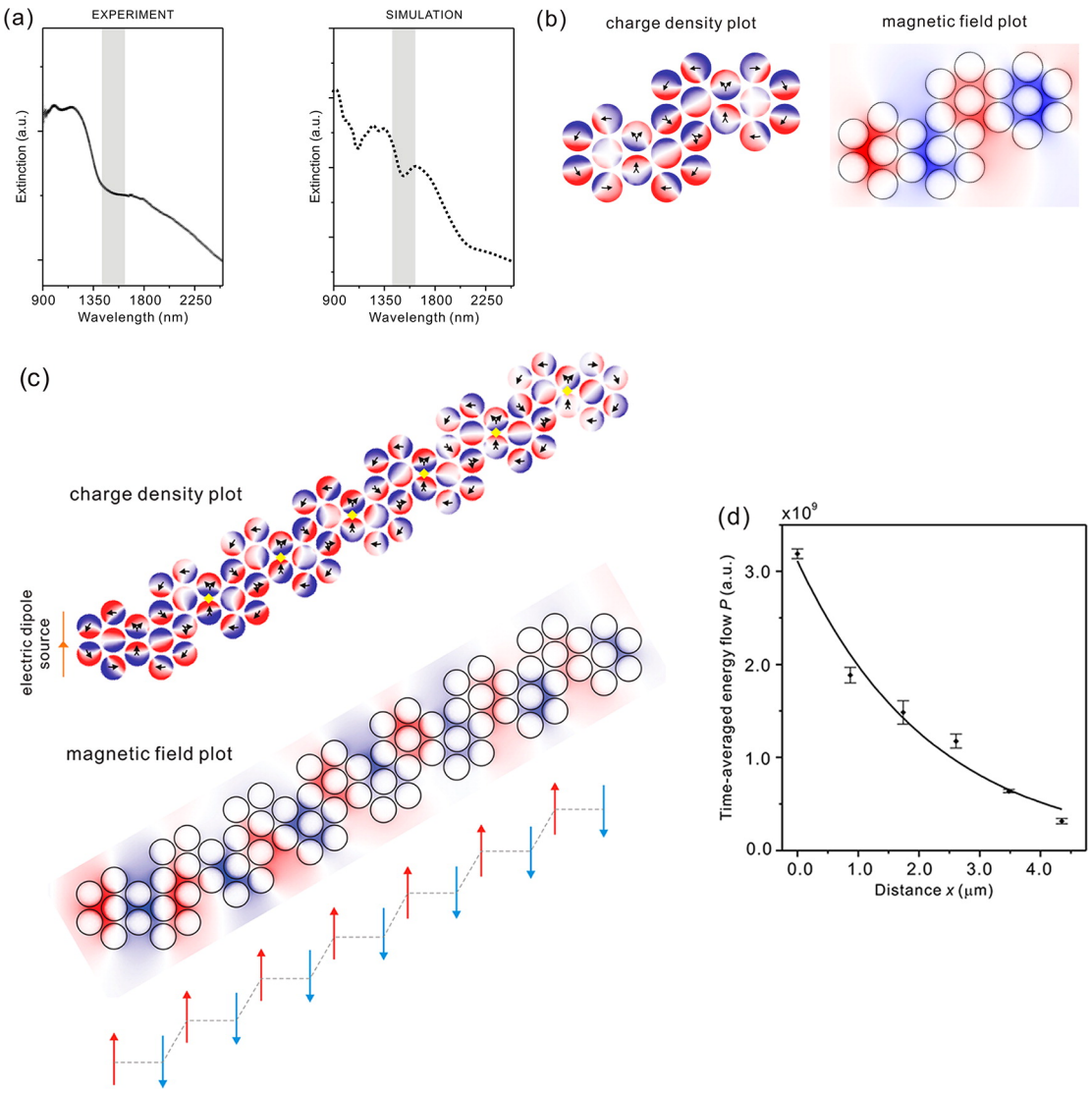

Figure 5.2 : (a) Experimental and simulated extinction spectra of the plasmonic chrysene structure. The magnetic resonance is highlighted by the shaded region around 1500 nm. (b) Simulated charge density and magnetic field plots at 1500 nm. (c) Charge density simulation of amagnetic plasmon steererwith 14 heptamer units along a zigzag chain. An electric dipole source with an amplitude of 1×10^{-9} mA is placed 150 nm in front of the leftmost heptamer. (d) Energy flow as a function of distance fromthe location of excitation. The energy flow values were taken at the heptamer junctions marked with yellow diamonds in (c). The junctions at the twoends of the chainwere excluded in the fitting in order to avoid influence fromlight scattering. The half-length of each error bar was defined as the difference between a full and a half-mesh calculation. Some error bars are too small to visualize clearly. The fitted energy flow equation is $P = 3.1 \times 10^9 exp(-x/2.2)$, which corresponds to a field decay length of $2.2\mu m$.

strate was taken as 2.1, and the empirical dielectric function of bulk gold (Johnson and Christy) was used.[47] The chromium layer was not included in the simulations because it only slightly weakens the spectral response and does not change the underlying physics. The experimental spectrum shows good qualitative agreement with the simulated spectrum. Differences are likely due to inhomogeneous broadening in the ensemble measurement caused by fabrication tolerances. Nevertheless, all of the main spectral features including the two distinct resonance dips are clearly observed in the experiment.

To further investigate the underlying physics, electromagnetic field plots were generated at 1100 and 1500 nm. The shorter wavelength at 1100 nm is associated with a multiple Fano resonance mode, in which each heptamer exhibits a Fano resonance field distribution (not shown). Here the longer wavelength feature at 1500 nm is our primary interest (shaded region in Figure 5.2a). The simulated charge density plot at this resonance is presented in Figure 5.2b, which shows ring currents circulating in opposite directions around the four heptamers. Despite the fact that there is an offset in the structure, i.e., two heptamers are twisted with respect to the other two, the gold nanoparticles shared between each neighboring heptamer pair work as a mutual link that couples the ring currents of the individual heptamers. The magnetic nature of this resonance can be identified more explicitly in the magnetic field plot, which shows the excited magnetic dipoles oscillating in antiparallel directions from one heptamer to the next (Figure 5.2b).

Using this plasmonic analogue of chrysene as a building block, we can construct a plasmon waveguide by extending more heptamer units along the twist direction. As shown in Figure 5.2c, this leads to a chain with zigzag features, and here, we have included a total of 14 heptamers along the entire chain. In our simulations, we excited the waveguide with an electric dipole source at the left end of the chain. Only the first heptamer is excited by the external source; all other heptamers in the chain become resonant due to the aforementioned coupling between neighboring heptamers. In the charge density plot of the heptamer currents flow successively via individual heptamers (Figure 5.2c). This excitation of antiphase ring currents is facilitated by the mutual links between neighboring heptamers. The resulting magnetic dipoles form an "antiferromagnetic" configuration, in which they are aligned alternatively antiparallel, enabling the propagation of magnetic plasmons along the entire chain. As a result, the energy from the dipole source can be transferred and steered via magnetic plasmon propagation along the zigzag chain, with bending features much smaller than the wavelength of light. Such a plasmon steerer could be very useful in applications where the transportation of plasmons requires a subwavelength profile as well as directional guidance.

Due to energy dissipation and light scattering, the electromagnetic field intensity decays continuously with increasing propagation distance, as evident in both the charge density and magnetic field plots. In order to characterize the efficiency of our magnetic plasmon waveguide, the time-averaged energy flow P was calculated along

the chain. The energy flow values were obtained at the individual junctions where the neighboring heptamers are joined. To minimize interference effects due to light scattering, the heptamer units near the two ends of the chain were excluded from the calculation.[84] The recorded junction positions are indicated by yellow diamonds in Figure 5.2c. The exponential fit yields a decay length of $2.2\mu m$ (Figure 5.2d), which corresponds to 4.4 unit cells. This decay length is slightly smaller than that of a linear heptamer chain ($2.65\mu m$),[60] and the difference can be attributed to the additional losses introduced by the zigzag corners. Nevertheless, this magnetic plasmon steerer shows a much better performance compared to electric plasmon propagation along a linear chain of closely spaced gold nanorods, which has a decay length of only 410 nm.[67] Their operating wavelength was 570 nm with a gold rod length of 90 nm, giving rise to a ratio of 6.3. In our case, the operating wavelength is 1500 nm and the particle size is 260 nm, corresponding approximately to a ratio of 6. Therefore, our magnetic plasmon waveguide and their electric plasmon waveguide are very similar regarding their subwavelength nature. In contrast to the electric plasmon waveguide based on a super-radiant electric mode, which suffers from significant dissipation, the radiation loss of our magnetic plasmon waveguide can be substantially suppressed. This low-loss characteristic results from the subradiant nature of the magnetic ring mode, which is only weakly coupled to light and therefore gives rise to much stronger field confinement for efficient plasmon propagation. Indeed, intrinsic losses in plasmonic nanostructures and inevitable imperfections in experiments can

lead to weaker coupling between neighboring heptamer units and therefore shorter propagation distances. To compensate for this, one can incorporate a gain medium such as quantum dots or use chemically prepared metallic nanoparticles, which have much higher quality factors and lower losses than evaporated gold nanostructures.

Next, we investigate the optical properties of the plasmonic triphenylene structure. The experimental and simulated extinction spectra for this structure are shown in Figure 5.3a. The experimental result is in good agreement with the simulation, but with a weaker response of the subradiant modes. When compared to the plasmonic chrysene structure, the simulated spectrum of the plasmonic triphenylene structure exhibits more complexity, specifically, multiple resonance dips. The resonance dips are approximately at 1100, 1300, 1500, and 1900 nm. In the following, we will again investigate the "antiferromagnetically" coupled resonance, which lies at approximately 1500 nm.

Previously, we demonstrated that the magnetic resonance for a conjugated heptamer maintains approximately the same wavelength for similar structures with different heptamer units.[58] Indeed, for the plasmonic triphenylene structure there is a small resonance dip at 1500 nm, which is highlighted by the shaded region in the simulated spectrum (Figure 5.3a). This resonance, however, is not clearly observable in the experiment. To provide further insight, the simulated absorption spectrum is also presented in Figure 5.3a. In this case, the structure is excited using an electric dipole source at the end of the leftmost heptamer. The resonances manifest them-

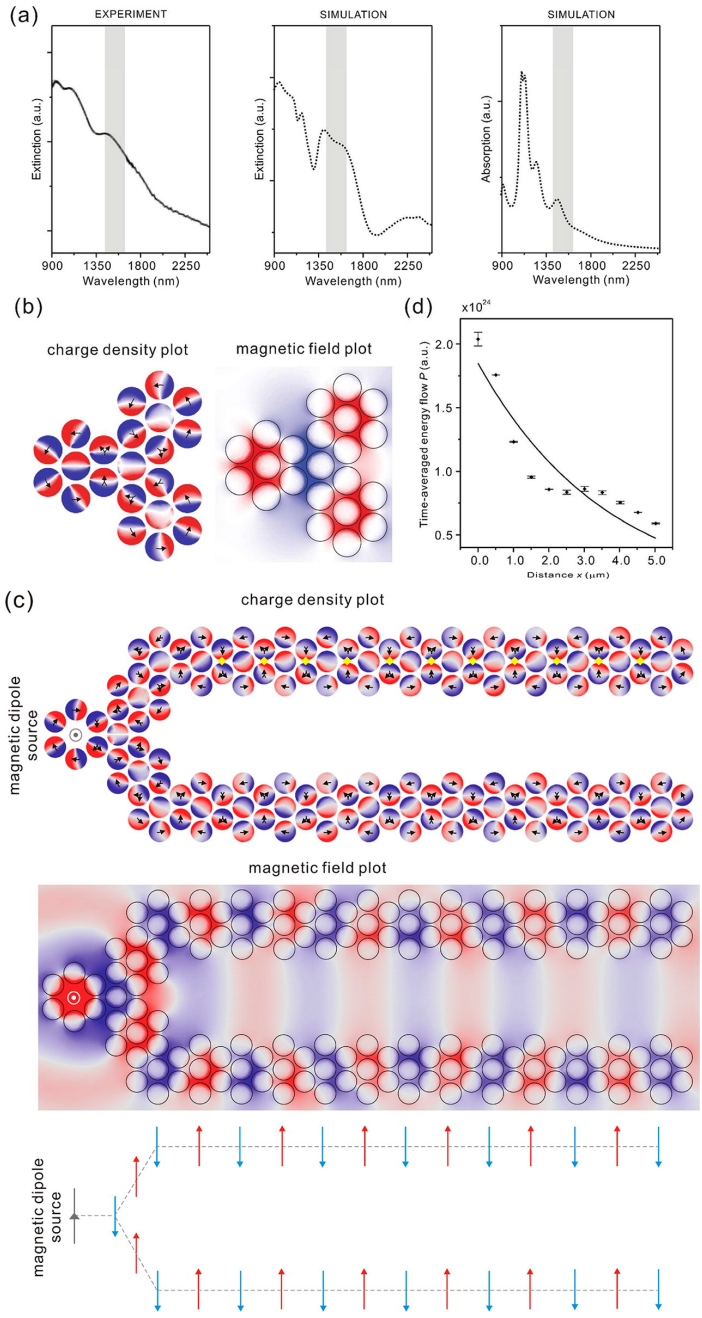

Figure 5.3 : (a) Experimental and simulated extinction spectra of the plasmonic triphenylene structure. The magnetic resonance is highlighted by the shaded region around 1500 nm. (b) Simulated charge density and magnetic field plots at the magnetic resonance. (c) Charge density simulation of a Y-shaped magnetic plasmon splitter with 30 heptamer units. A magnetic dipole source (represented by a concentric circle) with an amplitude of $1 \times 10^{-9} m^2 A$ is placed in the center of the leftmost heptamer by removing its center nanoparticle. (d) Energy flow as a function of distance from the location of excitation. The energy flow values were taken at the heptamer junctions marked with yellow diamonds in (c). The junctions at the two ends of the chain were excluded in order to avoid influence from light scattering. The half-length of each error bar was defined as the difference between a full and a half-mesh calculation. Some error bars are too small to visualize clearly. The fitted energy flowequation is $P = 1.8 \times 10^{24} exp(-x/3.7)$, corresponding to a field decay length of $3.7 \mu m$.

selves as absorption peaks in the spectrum. Specifically, the resonance at 1500 nm is more pronounced in the absorption spectrum than in the extinction spectrum. The charge density plot simulated at this resonance (Figure 5.3b) clearly demonstrates the excitation of alternating antiphase ring currents in the four fused heptamers. In particular, the central heptamer acts as a port, directing the current from the leftmost heptamer to the upper and lower heptamers. The corresponding magnetic field plot in Figure 5.3b shows that the magnetic dipole moment excited in the central heptamer oscillates in an antiparallel manner relative to the three outer heptamers. Owing to the high structural symmetry, the net electric dipole moment of this magnetic resonance is nearly zero, resulting in a dark mode. Such a dark mode is barely visible in the measurement under plane wave excitation at normal incidence, especially when considering the inhomogeneous broadening due to the variations of particle sizes and shapes over different unit cells in the sample. However, it is straightforward to identify this mode in the simulation when using an electric dipole as excitation source, due to its localized fields. The FTIR analysis was performed to provide more insight into understanding the physics of the magnetic modes. For practical applications of these plasmonic waveguides, a local excitation would be needed so that plasmons can propagate from the input end to the output end, performing the role of waveguiding.

We now extend the plasmonic triphenylene structure further by adding hepatamer units along the upper and lower branches. The resulting Y-shaped structure consists of 30 heptamers (Figure 5.3c). This allows us to examine another interesting excita-

tion scheme, which is unique to magnetic plasmon waveguides. We remove the center particle of the leftmost heptamer in the Y-splitter and place a magnetic dipole source in its center as the excitation source (see Figure 5.3c). The simulated charge density plot is presented in Figure 5.3c. The charge density plot clearly demonstrates the formation and propagation of antiferromagnetic- like magnetic plasmons in the waveguide. Ring currents generated from the first heptamer are split at the second heptamer and subsequently flow along the two separate linear heptamer branches. The fully antiparallel arrangement of the excited magnetic dipole moments can be seen clearly in the magnetic field plot in Figure 5.3c. To quantify the field decay length, we calculated the time-averaged energy flow P at individual junctions along one of the heptamer branches. Due to the intense light scattering and interference effects, the junctions at the two ends of the chain were excluded from this calculation.[84] The recorded junction positions are indicated by the yellow diamonds in the charge density plot in Figure 5.3c. The analysis reveals a field decay length of $3.7\mu m$ (Figure 5.3d), corresponding to 7.4 unit cells, which elucidates excellent subwavelength waveguiding performance.

A plasmon Y-splitter can also be used to converge propagating magnetic plasmons from two independent optical paths. In particular, the plasmon propagation can be switched on and off by changing the relative number of the heptamers in the two paths. In Figure 5.4a, the upper and lower branches contain the same number of heptamers (six in each). In Figure 5.4b, the upper and lower branches have

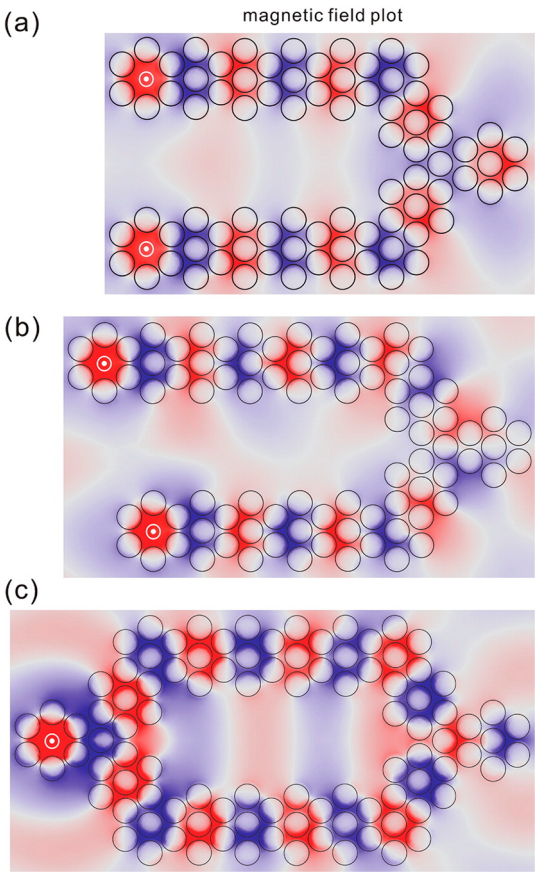

Figure 5.4 : Simulated magnetic field plots of plasmonic Y-splitters for constructive (a) and destructive (b) interference of magnetic plasmons, respectively. In (a), the two branches have an identical number of heptamers. In (b), the upper branch has one more heptamer than the lower branch. (c) Plasmonic Mach-Zehnder interferometer constructed by using two consecutive Y-spliters for splitting and converging magnetic plasmons. The magnetic dipole sources are driven in phase and represented by concentric circles in all cases.

seven and six heptamers, respectively. In both cases, two in-phase magnetic dipole sources are placed in the centers of the heptamers at the left ends by removing their center nanoparticles. As shown by the simulated magnetic field plot in Figure 5.4a, when each branch has the same number of heptamers, the magnetic plasmons propagate with the same phase and converge with constructive interference at the center heptamer of the plasmonic triphenylene vertex structure at the right end. The magnetic plasmons then continue to propagate forward, corresponding to an "ON" state. In contrast, when the upper branch has one more heptamer than the lower branch (Figure 5.4b), the structure yields antiphase magnetic plasmons, which result in destructive interference at the triphenylene structure at the right and no propagation beyond this structure. This situation thus corresponds to an "OFF" state. The "ON" and "OFF" states of the magnetic plasmon propagation strongly depend on the parity of the heptamer number difference between the two paths. More generally, when the difference between the number of heptamers in each branch is even or odd, the structure is in the "ON" or "OFF" state, respectively. The logic functions of the device can also be altered by changing the relative polarization of the excitation sources.[105] For out-of-phase magnetic dipole excitations, the situation is reversed: for chain lengths differing by an even number of heptamer units, destructive interference at the vertex results in plasmon annihilation and an "OFF" state, while for chain lengths differingby anoddnumber of heptamer units, constructive interference at the vertex results in further propagation and an "ON" state.

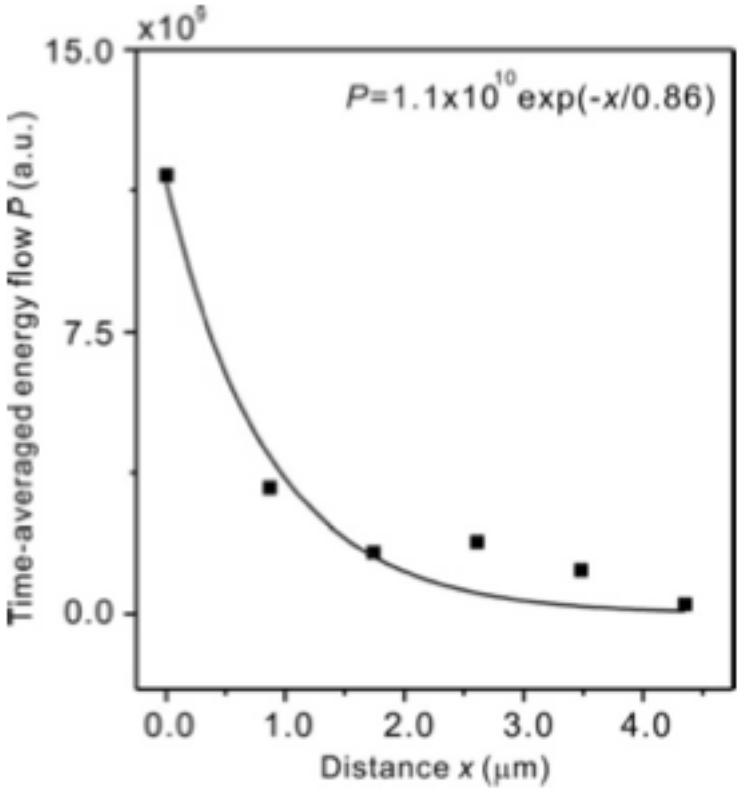

Figure 5.5 : Energy flow as a function of distance from the location of excitation for the electric plasmon mode. The fitted energy flowequation is $P = 1.1 \times 10^{10} exp(-x/0.86)$, corresponding to a field decay length of $0.86 \mu m$.

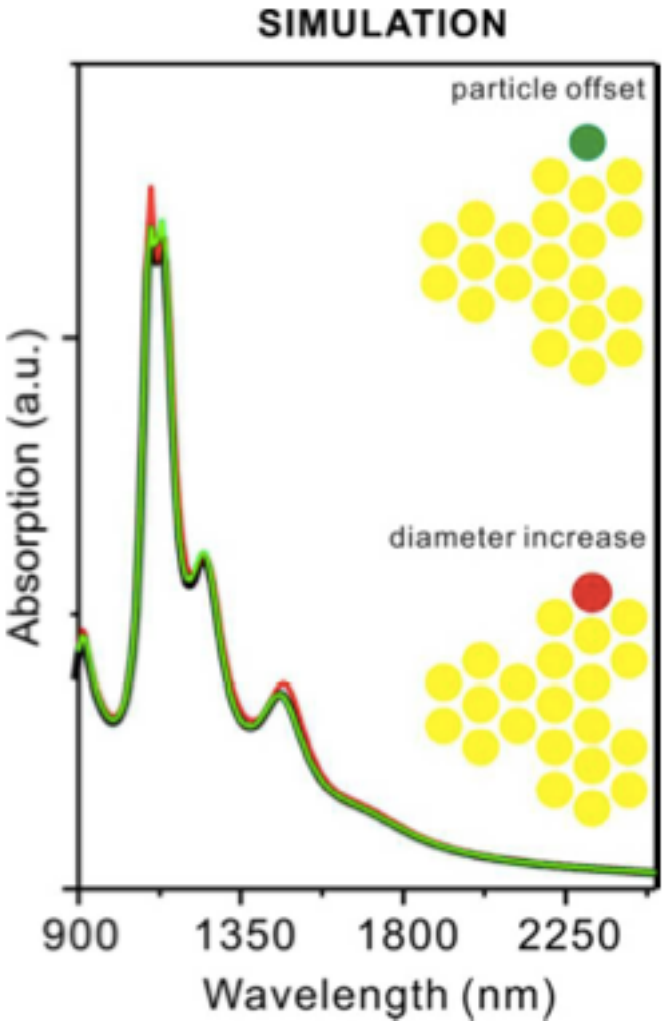

Figure 5.6 : Absorption spectra calculated from symmetry broken structues, comparing the symmetric structure (black curve) from Figure 5.3a, structure with one particle 10 nm upwards (green curve) and structure with one particle of 10 nm larger diameter (red curve).

Two consecutive Y-splitters can be used to construct a Mach-Zehnder interferometer, as shown in Figure 5.4c. The simulated magnetic field plot shows that the magnetic plasmons excited by themagnetic dipole source at the leftmost heptamer propagate through the first triphenylene intersection and subsequently are split into the two branches. The magnetic plasmons then propagate along the twoindependent optical paths and converge at the second triphenylene intersection, where constructive interference occurs. The magnetic plasmons then continue to propagate in the forward direction. This entire structure constitutes a plasmonic MachZehnder interferometer, which can be widely applicable for splitting signals in optical circuits.

Before we move on to the conclusions, as supplemental information, we calculated the propagation lengths of the magnetic and electric plasmons in the zigzag structure in Figure 5.2c. The propagation length of the electric plasmons is $0.86\mu m$ (see Fig 5.5), whereas that of the magnetic plasmons is $2.2\mu m$ (see Figure 5.2d), which is much longer.

Moreover, to demonstrate the robustness of our simulations, we have performed additional calculations for slight symmetry broken structures as shown in the right figure. The black curve is taken from Figure 5.3a. The green curve corresponds to the case in which one particle is offset by 10 nm upwards. The red curve corresponds to the case in which one particle's diameter is increased by 10 nm. It clearly shows that the simulations are not particularly sensitive to small structural variations.

5.3 Summaries and conclusions

In summary, we have demonstrated magnetic plasmon propagation in metallic nanocluster networks. Our magnetic plasmon waveguides exhibit long propagation lengths, significant subwavelength character, and rich functionalities. We have presented examples of several magnetic plasmon waveguiding devices including a plasmon steerer, a splitter, and a Mach-Zehnder interferometer. The manipulation of magnetic plasmons in heptamer interconnects can further be expanded to more complex systems, for example, by integrating more optical paths to achieve multipleinput and output plasmonic networks.[32] With their compact dimensions, outstanding low-loss propagation characteristics, and range of functionalities, magnetic plasmon-based devices based on these structures should be key to the further development of highperformance energy transport components in information processing and data storage applications.[72]

Chapter 6

Conclusion

In the thesis, with the help of FEM and FDTD based calulations, by commerical softwares such as COMSOL and Lumerical FDTD, we investigated nanoparticles of various different geometries. Manipulation of energy propagation, redirection, and dissipation can be achieved by investigating and designing tunable plasmonic nanostructures.

Regarding to the plasmonic dissipation mechanism, we brought up a brand-new improved damped harmonic oscillator model, where a geometrical dependent factor was included. This dynamic depolarization term explains well about the geometry dependent dissipation mechanism in the plasmonic systems. The FDTD calculations present the differences in the nanoshell and nanorods, in which we observed narrower linewidth from nanorods, making it a promising candidate for optical applications. Moreover, the FDTD calculation agreed well with our damped HO models in predicting the optical properties of different plasmonic nanosystems. This new model, compared to previous models, provides more accurate and complete understanding of the energy dissipation in plasmonic systems, and will be of great guidance for optical designs.

Next, we investigate the optical properties of elliptical nanorings with FEM and FDTD methods. We have demonstrated experimentally and theoretically that el-

liptical gold nanorings exhibited multiple plasmonic resonances. While lower-order resonances have large sensitivity with short detection limits, high-order resonances have mediate sensitivity with microscale detection length. These unique properties have been utilized for mutil-functional sensors and potentially for label-free imaging device. While only odd-mode resonances are visible at normal incidence, both odd- and even-mode resonances become visible at oblique incidence. The excitation of even-mode or dark-mode resonances is not only dependent on the incidence angle but also on the size and aspect ratio of ERs. Exeprimental and simulation data indicate that the excitation of dark-mode resonances is the result of the phase retardation. We also show that the intensities of the plasmonic resonances varies with the incidence angle. Moreover, a standing-waving model to quantitatively analyze all multiple resonances, which provided a simple designing guideline for the potential application of these structures to sensors and diagnosis.

We further use the numerical simulation method (FEM) to analyze the light-bending nanocups. As a very promising and interesting nanosystem, nanocup poesses unique light-redirection properties. We examined the spectral- and angle-dependent light-scattering properties of plasmonic nanocups. The transverse and axial plasmon modes of a nanocup scatter light in distinct angular patterns that are sensitive to the presence of a dielectric substrate and its local permittivity adjacent to the nanoparticle. On low-dielectric substrates, both the axial and transverse nanocup modes scatter light in directions determined by nanocup orientation. With a high degree of sensi-

tivity, the permittivity of the underlying substrate affects not only the wavelength of the resonances but also the angular light scattering of the system in significant ways. The different angular scattering and wavelength response from the axial and transverse nanocup modes make the nanocup an interesting particle for the nanoscale manipulation of light in three dimensions. The sensitivity of this system to geometric and environmental factors may present opportunities for active, substrate-mediated control of light scattering.

Last, by applying FEM mthod, we proved that neighboring fused heptamers can support magnetic plasmons due to the generation of antiphase ring currents in the metallic nanoclusters. We use such artificial plasmonic molecules as basic elements to construct low-loss plasmonic waveguides and devices. These magnetic plasmon-based complexes exhibit waveguiding functionalities including plasmon steering over large-angle bends, splitting at intersections, and MachZehnder interference between consecutive Y-splitters. The long field decay length as well as the significant sub-diffraction character may enable magnetic plasmon waveguides to be developed as primary components of nanoscale photonic devices with potential applications in energy transport, data storage, near-field microscopy, and so forth.

ss

Bibliography

[1] Amsden J. J. Kaplan D. L. Omenetto F. G. Hong M. K. Erramilli S. Altug H. Adato R., Yanik A. A. *Proc. Natl. Acad. Sci. U.S.A.*, 106:S19227, 2009. 18

[2] Sutherland D. S. Kall M. Bryant G. W. Garcia de Abajo F. J. Aizpurua J., Hanarp P. *Phys. Rev. Lett.*, 90:057401, 2003. 19, 22

[3] Lindsey J E Anderson, Courtney M Payne, Yu-Rong Zhen, Peter Nordlander, and Jason H Hafner. A Tunable Plasmon Resonance in Gold Nanobelts. *Nano letters*, 11(11):5034–5037, November 2011. 5

[4] Foley J. T. Arnoldus H. F. Transmission of dipole radiation through interfaces and the phenomenon of anti-critical angles. *J. Opt. Soc. Am.*, 21:1109, 2004. 58

[5] Altug H. Artar A., Yanik A. A. Multispectral plasmon induced transparency in coupled meta-atoms. *Nano Lett.*, 11:1685, 2011. 74

[6] Polman A. Atwater H. A. Plasmonics for improved photovoltaic devices. *Nat. Mater.*, 9:205, 2010. 53

[7] Maier S. A. Pendry J. B. Aubry A., Lei D. Y. Plasmonic hybridization between nanowires and a metallic surface: A transformation optics approach. *ACS Nano*, 5:3293, 2011. 54

[8] Barnes W. L. Auguie B. *Opt. Lett.*, 34:401, 2009. 27

[9] Crozier K. B. Banaee M. G. *Opt. Lett.*, 35:760, 2010. 19

[10] Qin L. Mirkin C. A. Banholzer M. J., Millstone J. E. *Chem. Soc. Rev.*, 37:885, 2008. 18

[11] Craig F Bohren and Donald R Huffman. *Absorption and Scattering of Light by Small Particles*. John Wiley & Sons, 1 edition, April 1983. 11, 12

[12] Devaux E. Laluet J. Y. Ebbesen T. W. Bozhevolnyi S., Volkov V. S. Channel plasmon subwavelength waveguide components including interferometers and ring resonators. *Nature*, 440:508, 2006. 74

[13] Atwater H. A. Brongersma M. L., Hartman J. W. Electromagnetic energy transfer and switching in nanoparticle chain arrays below the diffraction limit. *Phys. Rev. B*, 62:R16356, 2000. 75

[14] Maury P. A. de Boer M. Kuipers L. Huskens J. Reinhoudt D. N. Bruinink C. M., Peter M. *Adv. Funct. Mater.*, 16:1555, 2006. 47

[15] Rostislav Bukasov, Tamer A. Ali, Peter Nordlander, and Jennifer S Shumaker-Parry. Probing the Plasmonic Near-Field of Gold Nanocrescent Antennas. *Acs Nano*, 4(11):6639–6650, November 2010. 5

[16] Shumaker-Parry J. S. Bukasov R. *Anal. Chem.*, 81:4531, 2009. 18, 19

[17] Polman A. Catchpole K. R. Plasmonic solar cells. *Opt. Express*, 16:21793, 2008. 53, 63

[18] Kim Y.-S. Bur J. A. Shenoi R. V. Krishna S. Huang D. Lin S.-Y. Chang C.-C., Sharma Y. D. A surface plasmon enhanced infrared photodetector based on inas quantum dots. *Nano Lett.*, 10:1702, 2010. 53

[19] Chiang T. W.-Cheng K. W. Chiu W. T. Lee S. F. Liou Y. Yao Y. D. Chang L. J., Yu C. *J. Appl. Phys.*, 103:07C514, 2008. 19

[20] Slaughter L. S. Link S. Chang W.-S., Ha J. W. Plasmonic nanorod absorbers as orientation sensors. *Proc. Natl. Acad. Sci. U.S.A.*, 107:2781, 2010. 54

[21] Yen T.-J. Chen C.-Y., Wu S.-C. *Appl. Phys. Lett.*, 93:034110, 2008. 18, 28, 40

[22] Zhang S. Jin Z.-Yang B. Wang J. Chen H., Ming T. Effect of the dielectric properties of substrates on the scattering patterns of gold nanorods. *ACS Nano*, 5:4865, 2011. 54, 60

[23] Hill R. T. Chilkoti A. Smith D. R. Lazarides A. A. Chen S.-Y., Mock J. J. Gold nanoparticles on polarizable surfaces as raman scattering antennas. *ACS Nano*, 4:6535, 2010. 54, 60

[24] Xue C. Banholzer M. J. Schatz G. C. Mirkin C. A. Chen X., Li S. Plasmonic focusing in rod-sheath heteronanostructures. *ACS Nano*, 3:87, 2009. 53

[25] Rogers J. A. Choi K. M. *J. Am. Chem. Soc.*, 125:4060, 2003. 49

[26] Khang D.-Y. Jiang H. Huang Y. Y. Rogers J. A. Choi W. M., Song J. *Nano Lett.*, 7:1655, 2007. 50

[27] Cooper J. M. Clark A. W. *Adv. Mater.*, 22:4025, 2010. 19

[28] Cumming D. R. S. Cooper J. M. Clark A. W., Glidle A. *J. Am. Chem. Soc.*, 131:17615, 2009. 18, 19

[29] Ford M. Cortie M. *Nanotechnology*, 18:235704, 2007. 54, 57

[30] Park Y.-S. Bartal G. Zhang X. Cubukcu E., Zhang S. Split ring resonator sensors for infrared detection of single molecular monolayers. *Appl. Phys. Lett.*, 95:043113, 2009. 54

[31] C Dahmen, B Schmidt, and G von Plessen. Radiation damping in metal nanoparticle pairs. *Nano letters*, 2007. 6

[32] Giessen H. Dregely D., Hentschel M. Excitation and tuning of higher-order fano resonances in plasmonic oligomer clusters. *ACS Nano*, 5:8202, 2011. 91

[33] Brandl Daniel W. Park Tae-Ho Nordlander Peter Dutta C. M. A., Tamer A. *J. Chem. Phys.*, 129:084706/1, 2008. 22

[34] J A Fan, C Wu, K Bao, J Bao, R Bardhan, and N J Halas. Self-assembled plasmonic nanoparticle clusters. *science*, 2010. 5

[35] Bao K. Bao J. M.-Bardhan R. Halas N. J. Manoharan V. N. Nordlander P. Shvets G. Capasso F. Fan J. A., Wu C. H. Self-assembled plasmonic nanoparticle clusters. *Science*, 328:1135, 2010. 74

[36] François Flory, Ludovic Escoubas, and Gérard Berginc. Optical properties of nanostructured materials: a review. *Journal of Nanophotonics*, 5(1):052502, 2011. 5

[37] Martin O. J. F. Gallinet B. Influence of electromagnetic interactions on the line shape of plasmonic fano resonances. *ACS Nano*, 5:8999, 2011. 74

[38] Cabrini S. Schuck P. J. Leone S. R. Habteyes T. G., Dhuey S. *Nano Lett.*, 11: 1819, 2011. 23

[39] N J Halas, S Lal, S Link, and W S Chang. A Plethora of Plasmonics from the Laboratory for Nanophotonics at Rice University - Halas - 2012 - Advanced Materials - Wiley Online Library. *Advanced Materials*, 2012. 5

[40] Ali T. A. Sutherland D. S. Nordlander P. Hao F., Larsson E. M. *Chem. Phys. Lett.*, 458:262, 2008. 19, 23

[41] Tsang J. C. Hartstein A., Kirtley J. R. Enhancement of the infrared absorption from molecular monolayers with thin metal overlayers. *Phys. Rev. Lett.*, 45:201, 1980. 53

[42] Vogelgesang R. Giessen H. Alivisatos A. P. Liu N. Hentschel M., Saliba M. Transition from isolated to collective modes in plasmonic oligomers. *Nano Lett.*, 10:2721, 2010. 74

[43] Vogelgesang R. Giessen H. Liu N. Hentschel M., Dregely D. Plasmonic

oligomers: The role of individual particles in collective behavior. *ACS Nano*, 5: 2042, 2011. 53

[44] Seok T. J. Lee S. Hafner J. H. Drezek R. A. Choo H. Hu Y. S., Jeon J. Enhanced raman scattering from nanoparticle-decorated nanocone substrates: A practical approach to harness in-plane excitation. *ACS Nano*, 4:5721, 2010. 54

[45] John David Jackson. *Classical Electrodynamics Third Edition*. Wiley, 3 edition, August 1998. 8

[46] Sabarinathan J. Jiang H. *J. Phys. Chem. C*, 114:15243, 2010. 19, 27

[47] Christy R. W. Johnson P. B. Optical constants of the noble metals. *Phys. Rev. B*, 6:4370, 1972. 69, 79

[48] Nicholas S King, Yang Li, Ciceron Ayala-Orozco, Travis Brannan, Peter Nordlander, and Naomi J Halas. Angle- and Spectral-Dependent Light Scattering from Plasmonic Nanocups. *Acs Nano*, 5(9):7254–7262, September 2011. 5

[49] Lassiter J. B. Nordlander P. Halas N. J. Knight M. W., Wu Y. Substrates matter: Influence of an adjacent dielectric on an individual plasmonic nanoparticle. *Nano Lett.*, 9:2188, 2009. 56, 61, 63

[50] Tsukruk V. V. Ko H., Singamaneni S. *Small*, 4:1576, 2008. 18

[51] Novotny L. *Phys. Rev. Lett.*, 98:266802, 2007. 28, 58

[52] Kaell M. Sutherland D. S. Larsson E. M., Alegret J. *Nano Lett.*, 7:1256, 2007. 19

[53] hernandez L. I. Brandl D. W. Romero I. Lal S. Hafner J. H. Nordlander P. Halas N. J. Lassiter J. B., Aizpurua J. Close encounters between two nanoshells. *Nano Lett.*, 8:1212, 2008. 74

[54] Kim S.-H. Kim S. Yang S.-M. Lee S. Y., Jeong J.-R. *Langmuir*, 25:12535, 2009. 47

[55] Tay L. Cui B.-Geissler M. Veres T. Li K., Clime L. *Anal. Chem.*, 80:4945, 2008. 19

[56] Yang T. Castellana E. T. Chen J. Cremer P. S. Liao W.-S., Chen X. *Biointerphases*, 4:80, 2009. 18

[57] S Linic, P Christopher, and D B Ingram. Plasmonic-metal nanostructures for efficient conversion of solar to chemical energy. *Nature materials*, 2011. 5

[58] Na Liu, Shaunak Mukherjee, Kui Bao, Yang Li, Lisa V. Brown, Peter Nordlander, and Naomi J. Halas. Manipulating magnetic plasmon propagation in metallic nanocluster networks. *ACS Nano*, 6(6):5482–5488, 2012. doi: 10.1021/nn301393x. URL `http://pubs.acs.org/doi/abs/10.1021/nn301393x`. 82

[59] Wu D. M. Liu Y. M. Steele J. M. Sun C. Zhu S. N. Zhang X. Liu H., Genov

D. A. Magnetic plasmon propagation along a chain of connected subwavelength resonators at infrared frequencies. *Phys. Rev. Lett.*, 97:243902, 2006. 76

[60] Bao K. Brown L. V. Dorfmueller J. Nordlander P. Halas N. J Liu N., Mukherjee S. Magnetic plasmon formation and propagation in artificial aromatic molecules. *Nano Lett.*, 12:364, 2012. 75, 81

[61] Giessen H. Liu N. Coupling effects in optical metamaterials. *Angew. Chem.,Int. Ed.*, 49:9838, 2010. 76

[62] Giessen H. Liu N., Kaiser S. Magnetoinductive and electroinductive coupling in plasmonic metamaterial molecules. *Adv. Mater.*, 20:4521, 2008. 54, 74

[63] Kunz R. E. Lukosz W. Light emission by magnetic and electric dipoles close to a plane dielectric interface. ii. radiation patterns of perpendicular oriented dipoles. *J. Opt. Soc. Am.*, 67:1615, 1977. 58

[64] Maier S. A. Halas N. J. Nordlander P. Giessen H. Chong C. T. Lukyanchuk B., Zheludev N. I. The fano resonance in plasmonic nanostructures and metamaterials. *Nat. Mater.*, 9:707, 2010. 74

[65] Moskovits M. Surface-enhanced spectroscopy. *Rev. of Mod. Phys.*, 57:783, 1985. 53

[66] Atwater H. A. Maier S. Plasmonics: Localization and guiding of electromagnetic energy in metal/dielectric structures. *J. Appl. Phys.*, 98:011101, 2005. 76

[67] Atwater H. A. Meltzer S. Harel E. Koel B. E. Requicha A. A. G. Maier S. A., Kik P. G. Local detection of electromagnetic energy transport below the diffraction limit in metal nanoparticle plasmon waveguides. *Nat. Mater.*, 2:229, 2003. 75, 81

[68] Kik P. G. Meltzer S Requicha A. G. Atwater H. A. Maier S. A., Brongersma M. L. Plasmonics-a route to nanoscale optical devices. *Adv. Mater.*, 13:1501, 2001. 76

[69] Halas N. J. Mirin N. A. Light-bending nanoparticles. *Nano Lett.*, 9:1255, 2009. 54, 55

[70] Kivshar Y. S. Miroshnichenko A. E.Lukyanchuk B., Maier S. A. Optically induced interaction of magnetic moments in hybrid metamaterials. *ACS Nano*, 6:837, 2012. 76

[71] A Moroz. Depolarization field of spheroidal particles. *JOSA B*, 2009. 8

[72] Engheta N. Circuits with light at nanoscales: Optical nanocircuits inspired by metamaterials. *Science*, 317:1689, 2007. 91

[73] Lovrincic R. Fahsold G. Pucci A. Aizpurua J. Cornelius T. W. Toimil-Molares M. E. Neumann R. Karim S. Neubrech F., Kolb T. *Appl. Phys. Lett.*, 89:253104, 2006. 28

[74] Weber D. Bochterle J. Shen H. Lamy de la Chapelle M.-Bryant G. W. Aizpurua

J. Pucci A. Neubrech F., Garcia-Etxarri A. *Appl. Phys. Lett.*, 96:213111, 2010. 23, 26

[75] P Nordlander. On the Energy Shift between Near-Field and Far-Field Peak Intensities in Localized Plasmon Systems - Nano Letters (ACS Publications). *Nano letters*, 2011. 8

[76] Westcott S. L. Halas N. J. Oldenburg S. J., Averitt R. D. Nanoengineering of optical resonances. *Chem. Phys. Lett.*, 288:243, 1998. 53, 56

[77] Westcott S. L. Halas N. J. Oldenburg S. J., Jackson J. B. Infrared extinction properties of gold nanoshells. *Appl. Phys. Lett.*, 75:2897, 2001. 56

[78] Carrascosa L. G. Gonzalez-Guerro A. B. Lechuga L. M.-Sepulveda B. Otte M. A., Estevez M.-C. Improved biosensing capability with novel suspended nanodisks. *J. Phys. Chem. C*, 115:5344, 2011. 54

[79] Nordlander P. *ACS Nano*, 3:488, 2009. 19, 23, 28

[80] Robbins D. J. Stewart W. J. Pendry J. B., Holden A. J. *IEEE Trans. Microwave Theory Tech.*, 47:2075, 1999. 19

[81] Trupke T. Zhang G. Zhao J. Green M. A. Pillai S., Catchpole K. R. Enhanced emission from si-based light-emitting diodes using surface plasmons. *Appl. Phys. Lett.*, 88:161102, 2006. 53

[82] Signorell R. Preston T. C. Growth and optical properties of gold nanoshells prior to the formation of a continuous metallic layer. *ACS Nano*, 3:3696, 2009. 53

[83] Halas N. J. Nordlander P. Prodan E., Radloff C. A hybridization model for the plasmon response of complex nanostructures. *Science*, 302:419, 2003. 74

[84] Krenn J. R. Aussenegg F. R. Quinten M., Leitner A. Electromagnetic energy transport via linear chains of silver nanoparticles. *Opt. Lett.*, 23:1331, 1998. 81, 85

[85] Hohenau A. Ditlbacher H. Leitner A. Aussenegg F. R. Schaich W. L. Puscasu I. Monacelli B. Boreman G. Schider G., Krenn J. R. *Phys. Rev. B*, 68:155427, 2003. 26

[86] Ringhofer K. H. Solymar L. Shamonina E., Kalinin V. A. Magneto-inductive waveguide. *Electron. Lett.*, 38:371, 2002. 76

[87] Schultz S. Shelby R. A., Smith D. R. *Science*, 292:77, 2001. 18

[88] Glidle A. Cooper J. M. Cumming D. R. S. Sheridan A. K., Clark A. W. *Appl. Phys. Lett.*, 90:143105, 2007. 18

[89] Schatz G. C. Van Duyne R. P. Sherry L. J., Chang S.-H. Localized surface plasmon resonance spectroscopy of single silver nanocubes. *Nano Lett.*, 5:2034, 2005. 54

[90] Kreiter M. Shumaker-Parry J. S., Rochholz H. *Adv. Mater.*, 17:2131, 2005. 19

[91] C Sönnichsen, T Franzl, T Wilk, G von Plessen, and J Feldmann. Drastic Reduction of Plasmon Damping in Gold Nanorods. *Physical Review Letters*, 88 (7), January 2002. 6

[92] Economou E. N. Soukoulis C. M., Kafesaki M. *Adv. Mater.*, 18:1941, 2006. 18

[93] Sun W. Fang N. Stender A. S., Wang G. Influence of gold nanorod geometry on optical response. *ACS Nano*, 4:7667, 2010. 53

[94] Shah N. C. Van Duyne R. P. Stiles P. L., Dieringer J. A. *Annu. Rev. Anal. Chem.*, 1:601, 2008. 18

[95] Zhang J. Li Y. Zhao Z. Zhang K. Zhang G. Guo J. Yang B. Sun Z., Li Y. *Adv. Funct. Mater.*, 18:4036, 2008. 44

[96] Mirin N. Halas N. J. Sundararajan S. P., Grady N. K. Nanoparticle-induced enhancement and suppression of photocurrent in a silicon photodiode. *Nano Lett.*, 8:624, 2008. 63

[97] Chang W.-S. Willingham B. Khanal B. P. Zubarev E. R. Link S. Swanglap P., Slaughter L. S. Seeing double: Coupling between substrate image charges and collective plasmon modes in self-assembled nanoparticle superstructures. *ACS Nano*, 5:4892, 2011. 54

[98] Kundu J.-Wang H. Halas N. J. Tam F., Chen A. L. Mesoscopic nanoshells: Geometry-dependent plasmon resonances beyond the quasistatic limit. *J. Chem. Phys.*, 127:204703, 2007. 56

[99] S J Tan, M J Campolongo, D Luo, and W Cheng. Building plasmonic nanostructures with DNA. *Nature Nanotechnology*, 2011. 5

[100] Lin J.-W. Lee P.-T. Tsai C.-Y., Lu S.-P. *Appl. Phys. Lett.*, 98:153108, 2011. 19, 22

[101] Mohammadi R. Retsch M.-Butt H.-J.-Landfester K. Weiss C. K. Kreiter M. Vogel N., Fischer J. *Nano Lett.*, 11:446, 2011. 27

[102] Chen K. Fromen Catherine A.-Betts Douglas E. Desimone Joseph M. Wang Y., Merkel Timothy J. *Langmuir*, 27:524, 2011. 49

[103] S C Warren and E Thimsen. Plasmonic solar water splitting. *Energy & Environmental Science*, 2012. 5

[104] Hong Wei, Alejandro Reyes-Coronado, Peter Nordlander, Javier Aizpurua, and Hongxing Xu. Multipolar Plasmon Resonances in Individual Ag Nanorice. *Acs Nano*, 4(5):2649–2654, May 2010. 5

[105] Tian X. R. Wang Z. X. Cong F. Z. Liu N. Zhang S. P. Nordlander P. Halas N. J. Xu H. X. Wei H., Li Z. P. Quantum dot-based local field imaging reveals

plasmon-based interferometric logic in silver nanowire networks. *Nano Lett.*, 11:471, 2011. 74, 87

[106] Nordlander P. Wu Y. Finite-difference time-domain modeling of the optical properties of nanoparticles near dielectric substrates. *J. Phys. Chem. C*, 114: 7302, 2010. 56, 61

[107] Rioux R. M. Perez-Castillejos R. Capasso F. Whitesides G. M. Xu Q., Bao J. *Nano Lett.*, 7:2800, 2007. 28, 29

[108] Yang P. Yan R., Gargas D. *Nat. Photonics*, 3:569, 2009. 18

[109] Lagae L. Maes G. Borghs G. Ye J., van Dorpe P. *Nanotechnology*, 20:465203, 2009. 19, 22, 28, 49

[110] Lodewijks K. Lagae L. Kawamura T. Van Dorpe P. Ye J., Shioi M. *Appl. Phys. Lett.*, 97:163106, 2010. 19

[111] Van Roy W. Lagae L. Maes G. Borghs G. Van Dorpe P. Ye J., Verellen N. Plasmonic modes of metallic semishells in a polymer film. *ACS Nano*, 4:1457, 2010. 54

[112] Van Roy W. Lodewijks K. De Vlaminck I. Maes G. Borghs G. Ye J., Van Dorpe P. Fabrication and optical properties of gold semishells. *J. Phys. Chem. C*, 113:3110, 2009. 54

[113] Lim S. H. Matheu P. Schaadt D. M. Yu E. T., Derkacs D. Plasmonic nanoparticle scattering for enhanced performance of photovoltaic and photodetector devices. *Proc. SPIE*, 7033:70331V, 2008. 53

[114] Qin D. Golden G. Wallace P. M. Yu Q., Guan P. *Nano Lett.*, 8:1923, 2008. 18

[115] Wang H. Zhang L. Cuprous oxide nanoshells with geometrically tunable optical properties. *ACS Nano*, 5:3257, 2011. 53

[116] Lassiter J. B. Halas N. J. Zhang Y., Barhoumi A. Orientation-preserving transfer and directional light scattering from individual light-bending nanoparticles. *Nano Lett.*, 11:1838, 2011. 54

[117] I Zorić, M Zäch, B Kasemo, and C Langhammer. Gold,platinum,and aluminum nanodisk plasmons: material independence,subradiance,and damping mechanisms. *Acs Nano*, 2011. 6

[118] J Zuloaga, E Prodan, and P Nordlander. Quantum description of the plasmon resonances of a nanoparticle dimer. *Nano letters*, 2009. 5